CRUSTAL SEISMIC ANISOTROPY AND STRUCTURE FROM TEXTURAL AND SEISMIC INVESTIGATIONS IN THE CYCLADIC REGION, GREECE

by

ÉLISE COSSETTE

B. Sc. University of Ottawa – Ottawa, Ontario, 2012

A THESIS SUBMITTED UNDER THE SUPERVISION OF
Pascal Audet and David Schneider

IN PARTIAL FULFILMENT OF THE REQUIREMENT FOR THE DEGREE OF

MASTER OF SCIENCE

in

The faculty of graduate and postdoctoral studies
Department of Earth Sciences

We accept this thesis as conforming to the required standard

UNIVERSITY OF OTTAWA

June 2015

© Élise Cossette, Ottawa, Canada, 2015

TABLE OF CONTENT

LIST OF FIGURES

Introduction (Chapter 1)

Article One (Chapter 2)

poles/crystallographic directions as equal-area, lower hemisphere projections. Small pole figure insets show the plane of foliation and the lineation for each sample. n_{gr} and n_{or} are the number of grains and orientations used in the density calculation, respectively.

Figure 2-5. Seismic wave velocity (triangles) and anisotropy (circles) profile with respect to structural position. Shallow depths are at the top of the diagram and the scale is highly approximate. On the velocity and anisotropy profiles, solid black line represents data for the P-wave and dashed line is for the S-wave. Dotted line represents values calculated for glaucophane bearing eclogite from Bezacier et al. (2010) with a density of 3.45 g/cm^3.

Figure 2-6. P-wave velocities and S-wave velocity anisotropies geographically oriented, using field structural measurements (plane of foliation and lineation on small stereonet). Data plotted on equal-area, lower hemisphere stereonets. Data for EC12-19 (blueschist) not shown since the sample was of a cm-scale fold. Samples exhibit a subvertical slow axis of wave propagation.

Article Two (Chapter 3)

Figure 3-1. Map of the Aegean region showing seismic station locations of the GE and Z3 networks and the West Cycladic Detachment System (WCDS).

Figure 3-2. Receiver functions and harmonic decomposition for station APE on Naxos (A and B) and station SANT on Santorini (C and D). The azimuth α is the orientation obtained when the variance is minimised on B||.

Figure 3-3. P-wave ray angle distribution at station APE superimposed on A: P-wave velocity (in km/s) and B: Vp/Vs ratio of metapelites in the Cyclades. The maximum and minimum velocities resolved by the P-rays are ~6.1 and ~5.9 km/s, respectively, giving a P-wave anisotropy of ~3.3%. Seismic figures are from Cossette et al. (2015) and represent data for one sample of the West Cycladic Detachment System.

Figure 3-4. Receiver functions for the 21 selected seismic stations in the Cyclades in function of A: time and B: depth.

Figure 3-5. Harmonic decomposition for the 21 selected seismic stations in the Cyclades. A-E: harmonic components A, B||, B⊥, C|| and C⊥. Dashed line on the term A harmonics corresponds to the Moho, and we note that it lies in the middle of a polarity reversal on the term B⊥.

Figure 3-6. A-F: Synthetic receiver functions (left) and harmonic decomposition (right) for models 1 to 6.

LIST OF TABLES AND SUPPLEMENTARY MATERIAL

Article One (Chapter 2)

Article Two (Chapter 3)

CRUSTAL SEISMIC ANISOTROPY AND STRUCTURE FROM TEXTURAL AND SEISMIC INVESTIGATIONS IN THE CYCLADIC REGION, GREECE

É. Cossette
University of Ottawa

ABSTRACT

In the first article, the seismic properties for a suite of rocks along the West Cycladic Detachment System (Greece) are calculated, using Electron backscatter diffraction (EBSD) measurements and the minerals' elastic stiffness tensors. Muscovite and glaucophane well defined crystallographic preferred orientation increases the seismic anisotropy. Maximum P-wave velocities have the same orientation as the Miocene extension and maximum S-wave anisotropy is subhorizontal, parallel with mineral alignment, suggesting strong radial anisotropy with a slow subvertical axis of symmetry. In the second article, teleseismic receiver functions are calculated for an array of stations in the Cyclades and decomposed into back-azimuth harmonics to visualise the variations in structure and anisotropy across the array. Synthetic receiver functions are modeled using the first order structural observations of seismic discontinuities and EBSD data. They indicate 5% of anisotropy with slow symmetry axis in the upper crust, and demonstrate the importance of rock textural constraints in seismic velocity profile interpretation.

ANISOTROPIE SISMIQUE ET STRUCTURE DE LA CROÛTE TERRESTRE À PARTIR D'ÉTUDES TEXTURALES ET SISMIQUES DANS LES CYCLADES, GRÈCE

Élise Cossette
Université d'Ottawa

RÉSUMÉ

Dans le premier article, les propriétés sismiques d'une suite de roches le long du Système de détachement des Cyclades occidentales (Grèce) sont calculées, en utilisant les mesures de diffraction d'électrons rétrodiffusés (EBSD) et les tenseurs élastiques de minéraux. L'orientation cristallographique préférentielle de la muscovite et du glaucophane augmente l'anisotropie sismique. Les vitesses maximales d'onde P ont la même orientation que celle de l'extension au Miocène, et l'anisotropie maximale d'onde S est subhorizontale, parallèle à l'alignement des minéraux, ce qui suggère une forte anisotropie radiale avec axe de symétrie lent. Dans le second article, les fonctions récepteur sont calculées pour une série de stations sismiques dans les Cyclades et sont décomposée en harmoniques d'azimut inverse, afin de visualiser les variations de structure et d'anisotropie à travers les Cyclades. Des fonctions récepteur synthétiques sont modélisées en employant les observations structurales de premier ordre des discontinuités sismiques et les données EBSD. Elles indiquent une anisotropie de 5% avec axe lent de symétrie dans la croute supérieure, et soulignent l'importance des contraintes de données texturales dans l'interprétation des profils sismiques.

ACKNOWLEDGMENTS/REMERCIEMENTS

I like to see the end of these last two years as the result of a complex equation in which several variables were essential. Funding for this research was provided by NSERC grants to both my supervisors Pascal Audet and David Schneider, as well as an Ontario Graduate Scholarship, a scholarship from Fonds du Recherche du Québec – Nature et Technologies and a Geological Society of America grant to myself.

Two irreplaceable variables: thank you to both my supervisors for giving me the opportunity of working on a challenging project – bridging geology and geophysics has been fulfilling in that it offered me a great variety of perceptions. Going up and down the mountains, literally and not, has been confronting though stimulating. I deeply appreciate the trust that has been put into myself. Thank you Dave for having believed in me and for wonderful discussions. Thank you Pascal for all your time and keeping me realise that simplicity is often the best choice.

This Master thesis is constructed as a series of two articles, and involved collaboration with the mentioned co-authors. Specific contributions include laboratory assistance from Gerlinde Habler for the Electron Backscatter Diffraction analyses in Vienna, and the use of a Python code for the synthetic teleseismic receiver functions written by Pascal Audet. Great discussions with David Schneider, Bernhard Grasemann, Pascal Audet and Benjamin Huet further helped me concretise this thesis. I would like to thank D. Mainprice and R. Hielscher for providing constructive advice about the MTEX software. I also would like to thank the local people of Kea, Kythnos and Sifnos for their warm hospitality, and Dr. E. Dempsey and an anonymous reviewer for valuable comments on the manuscript of the first paper.

My family has been extremely supportive and always believed my mind and heart would lead me the right way. Special thanks to Olivier who has been a constant variable in the equation and found incredible ways to make my burdens vanish.

As far as this thesis was about studying the physic Earth outside myself, it has also been a vast study of myself for which I am grateful.

“Ce n'était pas trop de toute une vie pour confronter l'un par l'autre ce monde où nous sommes et ce monde qui est nous.”
— Marguerite Yourcenar, L'œuvre au noir

1. INTRODUCTION

1.1 Seismic anisotropy

Seismic anisotropy, which is the directional dependence of seismic wave velocities, is an important phenomenon to study in order to understand crustal structure and dynamics. The theory of seismic anisotropy became interesting to geophysicists only in the eighties and nineties, mostly due to its application in detecting cracks for petroleum exploration. For the majority of investigations, the assumption was made of most media being isotropic since it necessitated much less computational complexity. However, most materials on Earth have elastic properties that vary with direction, making the Earth not completely anisotropic. Since nearly all geologic material possess preferred orientations, Helbig (1993) was prompted to assert that "wave propagation has to be assumed to be anisotropic unless (and until) it has been shown to be effectively isotropic" and "[W]ithout knowledge of the anisotropy we cannot correctly interpret seismic data".

Most media through which seismic waves propagate are considered to be elastic. In seismic anisotropy, it is the wave velocities that change with different directions of propagation in an elastic medium. Hooke's law describes how strain is related to stress in such linearly elastic material. The elastic constant is a fourth-rank elasticity tensor, C_{ijkl}, which relates the two second-rank tensors of strain ε and stress σ ($\sigma_{ij} = C_{ijkl}\varepsilon_{kl}$). The elastic stiffness tensor contains 81 components that determine the seismic wave velocities. Because of symmetry, it contains only 21 elements that are independent. Additional symmetries may also be considered, which further reduce the number of independent constants. Rock-forming minerals have different numbers of independent coefficients in the stiffness matrix, according to their crystallographic structure. A triclinic type of symmetry will therefore have 21 independent coefficients whereas a cubic type of symmetry will contain 3 of them, and an isotropic medium will contain only 2 of them (Anderson, 1989 and references therein). In seismology, most materials are considered with a hexagonal symmetry, since it is relatively simple and can approximate the alignment of minerals, with one preferred crystallographic direction that is the symmetry axis and all other crystallographic axes randomly oriented.

There are two main types of seismic anisotropy: transverse isotropy (or radial anisotropy) and azimuthal anisotropy. Transverse isotropy occurs in materials of hexagonal symmetry with a vertical symmetry axis. Seismic velocities in these media vary only with incidence angle, not with azimuth, meaning there is rotational symmetry about the vertical axis. A material with hexagonal symmetry for which the symmetry axis is horizontal is called azimuthally anisotropic.

Anisotropy can be achieved through different ways, such as the shape-preferred orientation of aligned fractures in the crust or of alternating fast and slow velocity material when the seismic wavelength is greater than the layering of crack spacing (e.g. Shearer, 2009). In such cases, the slow direction corresponds to the symmetry axis and the fast direction is parallel to the layers or the fractures. Aligned cracks constitute a strong source of azimuthal anisotropy observed in the upper crust (Shearer, 2009). Finally, the crystallographic preferred orientation (CPO) of minerals is also a strong contributor to seismic anisotropy, since seismic velocities may vary by tens of percent along the different crystallographic directions of a crystal (**Fig. 1-1**). Hexagonal anisotropy will be produced if the crystals are aligned with one main orientation (i.e. the symmetry axis). On the other hand, if crystals are randomly oriented in a rock, the elastic properties will be isotropic.

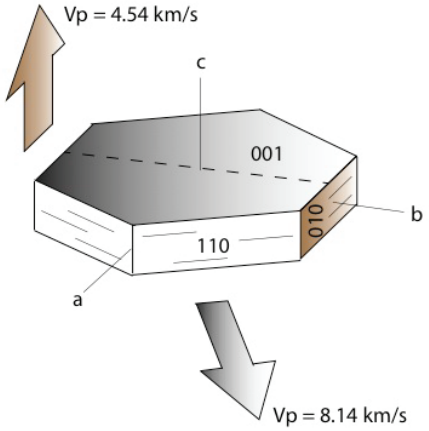

Figure 1-1. Muscovite crystal with varying P-wave velocities along planes (001) and (010)

Seismic anisotropy is quantified by calculating the differences between the slowest and the fastest P-wave or S-wave velocities (Vp and Vs, respectively). Vp anisotropy (AVp) and Vs anisotropy (AVs) are obtained with the following equations:

$$AVp = 200[(Vp_{max} - Vp_{min})/(Vp_{max} + Vp_{min})] \text{ and}$$
$$AVs = 200[(Vs1 - Vs2)/(Vs1 + Vs2)]$$

As shown in these equations, AVp is simply the difference between the slowest and highest velocities, which occur at different orientations in the mineral or rock. AVs is a little different in that shear waves split into fast and slow velocities along two normal polarising planes. This phenomenon is called shear wave splitting. The calculation for shear wave anisotropy thus takes into account these two velocities that are orthogonal. In the upper mantle, for example, the fast direction of P-wave corresponds to the polarization direction of the fastest S-wave (Shearer, 2009).

In the upper mantle, several studies reveal a relation between anisotropy from the alignment of crystal axes in olivine and the orientation of mantle flow (e.g. Babuska, 1972; Nicolas and Christensen, 1987 and references therein, Jung and Karato, 2001; Mainprice et al., 2005; Jung et al., 2014; Kim and Jung, 2014). Seismic anisotropy has often been found to be trench-normal in back-arc areas and trench-parallel in fore-arc areas, yet it also depends on the water content in olivine (Smith et al., 2001; Huang et al., 2011a, 2011b). Studying the variation of wave velocity therefore constitutes a strong approach to gain knowledge about deep crustal composition and structure. In the middle to upper crust, micas and amphiboles are the most anisotropic minerals susceptible to create observable seismic anisotropy (e.g. Ward et al., 2012; Tatham et al., 2008; Ji et al., 2013).

1.2 Methods of estimation

1.2.1 From textural analyses

One way to characterise the seismic anisotropy in the crust is by using rock samples and studying how the mineral CPO contributes to the observed anisotropy. This method has been widely used and interpreted in terms of rock composition and material deformation. Electron Backscatter Diffraction (EBSD) analyses allow to measure the crystallographic orientations of minerals within a rock sample. This technique uses a beam of electrons on a rock specimen and forms patterns of Kikuchi bands when the electrons are diffracted by crystal

planes – the Kikuchi bands corresponds to the diffracting planes (**Fig. 1-2**). These patterns describe the geometric orientation of crystals and are used afterwards for indexing (i.e. crystal orientation identification). The indexing normally necessitates only three crossing bands in order to give a unique solution of crystal orientation. The EBSD detector is used on a Scanning Electron Microscope (SEM), which allows characterising the chemistry of the minerals at the same time, for example using Energy-dispersive X-ray spectroscopy.

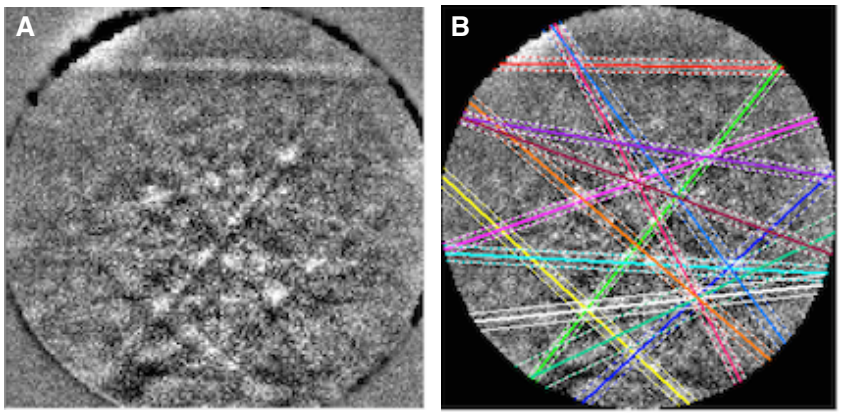

Figure 1-2. A: EBSD pattern with Kikuchi bands from the diffracting planes of a crystal and B: EBSD pattern during indexing of the Kikuchi bands

Every mineral is defined by a specific elastic stiffness tensor according to its crystal reference frame, which allows calculating the elastic properties of a single crystal, such as the wave velocities, the shear modulus, the Young's modulus, etc. In order to calculate the seismic wave velocities for rock specimens, one needs to calculate an average stiffness tensor that considers all minerals in the rock specimen with their right proportions. Most studies use mineral proportions as seen in petrographic analyses. However, the crystal reference frames generally do not coincide with the specimen reference frame. Using all the crystallographic orientations in a sample, it is possible to make the single crystal tensor reference frames coincide with the specimen in order to estimate an average tensor. We therefore use a Voigt-Reuss-Hill average of the matrices defining the single crystal stiffness tensors combined with the crystallographic orientations from EBSD data, and we obtain a new stiffness tensor for an aggregate of minerals, i.e. the rock specimen. This new tensor is used to calculate the elastic properties of the whole rock (detailed method in Mainprice et al., 2011).

Various softwares exist for EBSD data treatment. They are used to calculate average tensors as described previously, plot the crystallographic orientations and plot the elastic properties on stereonets in order to observe how the wave velocities, for example, vary with direction of incoming seismic rays. The crystallographic orientations are plotted on pole figures and represent the orientation of crystallographic directions (ex. [001] with brackets) or the poles to crystal planes (ex. (001) with parentheses). The lineation and plane of foliation of the corresponding rock are normally indicated in a pole figure so one can relate a preferred orientation of mineral to the fabric of the rock. The seismic properties such as the compressional and shear wave velocities, the Vp/Vs ratio and the shear wave anisotropy can also be plotted on a stereonet. It is therefore possible to see the presence or the absence of correlations between mineral CPO and seismic properties in function of orientation.

1.2.2 From seismic analyses

Seismic anisotropy can be observed through various techniques in seismology, such as shear wave splitting and receiver functions studies. The first phenomenon, described earlier in the introduction, is used to study the relation of mantle flow with plate tectonics. Fast polarizations that are aligned with the direction of plate motion were inferred, for example, to indicate simple shear at the base of the North American Plate (Fouch et al., 2000). At the East Pacific Rise, fast polarization was found to occur perpendicular to the mid-ocean ridge (Wolfe and Solomon, 1998). Shear wave splitting documents azimuthal anisotropy and yields robust fast polarization directions, however the plunges are not well resolved and thus it does not document radial anisotropy.

The receiver functions constitute a great technique to gain information about the Earth structure. This technique uses teleseismic data that contain signals from the source and from the propagation effect through the mantle and/or the crust, as well as diverse structures beneath a seismic station. The basic idea of receiver functions is the conversion of P- to S-waves (Ps waves) at discontinuities in seismic velocity in the crust (**Fig. 1-3a**). During this conversion, a part of the compressional energy is transformed into shear energy. The receiver functions are obtained by removing the signal from the earthquake and isolating the signal from the structure through which waves propagate. To do so, the Ps phase is isolated by

deconvolving the P pulse from the rest of the seismogram; the deconvolved form is termed the receiver function (**Fig. 1-3b**). One of the assumptions in this method is that the P component of wave motion is equal to the source wavelet.

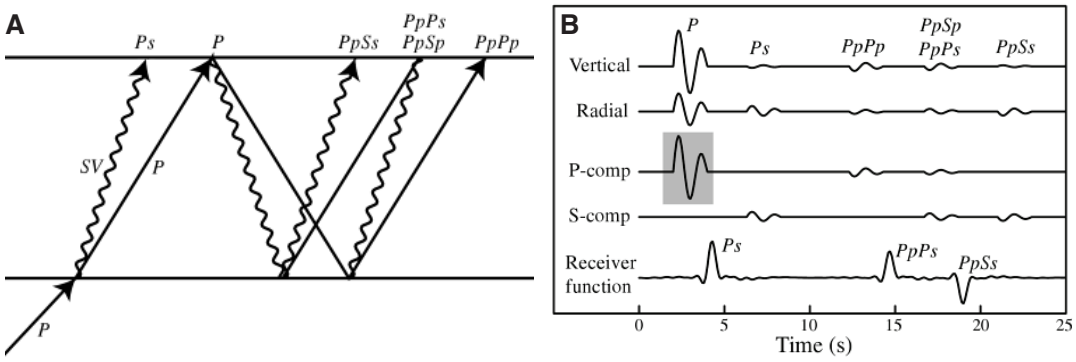

Figure 1-3. A: An upcoming P-wave generating an SV-polarised wave (Ps phase) when interacting with a discontinuity. B: Example of seismograms showing the response to an upcoming P-wave. The receiver function is obtained by deconvolving the P-pulse (gray window) from the S-component trace. Figures from *Shearer (2009)*

In general P-waves do not generate SH-waves (transverse component of shear), but only SV-waves (radial component of shear). The Ps phase is thus an SV-polarised wave, and for an isotropic and uniform crust containing horizontal discontinuities, energy would appear only on the SV-component of a seismogram. However, if the discontinuity is dipping, or if there is anisotropy, then the SH- or transverse component of shear may record energy from the Ps phase. Also, since S-waves travel slower than P-waves, they arrive after the direct P wave. Using a velocity model for a specific region, it is possible to calculate the depth of any boundaries from the time delay between the two pulses.

Receiver functions sample anisotropy differently based on the azimuth and incidence angle of the ray path. In fact, the radial component of shear may record differences in arrival time for the same structure, depending on the back-azimuth of the incoming P-wave (**Fig. 1-4a**). Moreover, the transverse component can show polarity reversals at a given time depending again on the back-azimuth of the incoming P-wave (**Fig. 1-4b**). In this case, the back-azimuth where there is a switch in polarity corresponds to the trend of the symmetry axis of anisotropy.

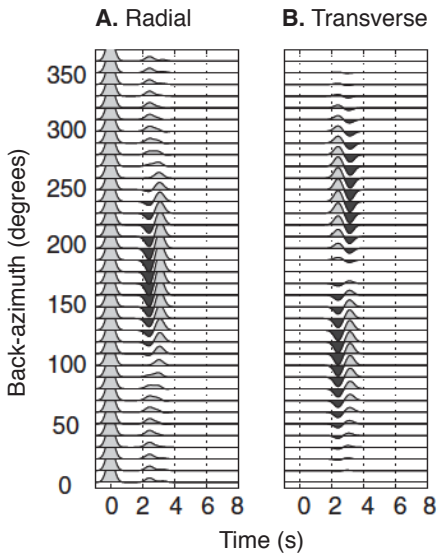

Figure 1-4. A: Radial component of shear showing variations in arrival time for the positive arrival between 2 and 4 seconds. B: Transverse component of shear showing polarity reversal at 180° back-azimtuh. Figure from *Porter et al., 2011*

In order to analyse the SV and SH components simultaneously and gain information of anisotropy or structural heterogeneity in function of back-azimuth, one can perform a harmonic decomposition of the receiver functions (method described in Bianchi et al., 2010; Agostinetti et al., 2011; Audet, 2015). It has been observed that for dipping interfaces, the amplitude of the transverse component as a function of back-azimuth forms two lobes (**Fig. 1-5**), and the same is observed with anisotropy with a plunging symmetry axis. This two-lobed pattern corresponds to a harmonic degree of 1. When the symmetry axis is horizontal,

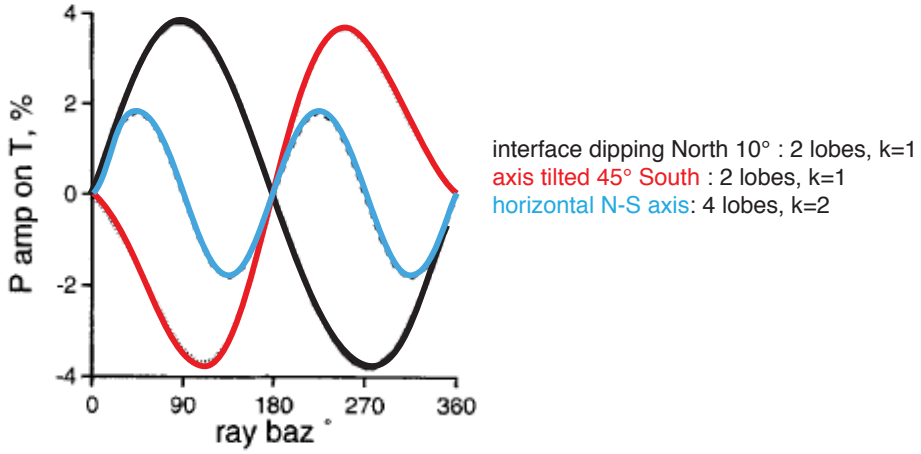

Figure 1-5. Amplitude of direct P-phase as function of ray back-azimuth. Amplitudes are expressed as a percentage of the maximum on the vertical component of a respective three-component seismogram, and expressed in percent. Figure from *Levin and Park, 1997*

it creates four lobes (**Fig. 1-5**), which corresponds to a harmonic degree of 2. The constant part of the SV component, which doesn't show any variation with back-azimuth, corresponds to a harmonic degree of zero. The energy due to anisotropic and/or dipping structures is thus separated from the isotropic signals and partitioned into the back-azimuth harmonics.

The harmonic decomposition expresses the sets of SV and SH into sums of cosine and sine as a function of the incoming wavefield direction. The resulting five harmonic terms (**Fig. 1-6**) represent the back-azimuth variations in the amplitude of SV and SH resolved onto each harmonic degree. The first term A represents the amplitude of the SV signal that does not vary with back-azimuth (k=0); it therefore represents signal originating from background velocity contrasts. The two terms B correspond to one periodicity with back-azimuth (k=1) for two normal orientations (B|| and B⊥), and indicate the presence of either a dipping interface or an anisotropic layer with a plunging symmetry axis. The two terms C correspond to two cycles with back-azimuth (k=2) and indicate anisotropy with a horizontal symmetry axis. Large amplitudes denote a preferential orientation with back-azimuth, and it is possible to find the azimuth corresponding to a maximum of energy on any component in order to get the strike of a dipping interface or the symmetry axis of anisotropy (Audet, 2015).

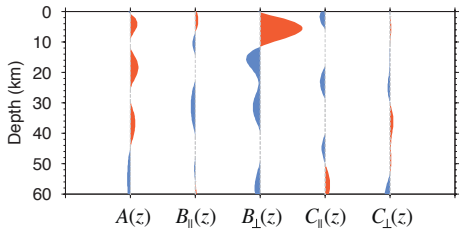

Figure 1-6. Example of harmonic decomposition of receiver functions, where each vertical trace corresponds to a harmonic in function of depth. Figure from *Audet 2015*

Receiver functions and their harmonic decomposition thus constitute a strong approach to estimate seismic anisotropy in the crust. Although the decomposition does not allow to discriminate between structural heterogeneity and anisotropy, it still gives a good idea of the substructures beneath seismic stations. A good knowledge of the tectonic setting, such as the recognition of large intra-crustal faults may allow favoring one phenomenon over the other.

1.3 Research purpose

Seismic anisotropy is gaining interest in the geoscientific community, as revealed by the increasing number of textural and seismic studies about rock physics and deformation in the upper mantle reveal. Nonetheless, there are still few studies about anisotropy in the shallower crust. In this contribution, we are interested in studying seismic anisotropy in the middle to upper crust by combining textural and seismic analyses. We focus our research on anisotropy generated by crystallographic preferred orientation (CPO) in minerals, and we ask ourselves: What is the contribution of CPO seismic anisotropy to seismic velocity profiles?

Our study is constructed as a series of two articles. The first paper (Chapter 2) therefore characterises the seismic properties of rock samples in the Cycladic region of Greece using textural analyses, and we find relations between the orientation of seismic anisotropy and the tectonic setting of this region. In order to resolve the contribution of this anisotropy to seismic profiles, the second article (Chapter 3) exposes a receiver function analysis of the Cyclades, from which we derive first order structural observations. We then model wave propagation through the crust using these structural constraints together with the textural constraints derived from the first article. The comparison of our synthetic receiver functions to the real ones reveals the importance of considering rock textures in the interpretation of seismic velocity profiles. The first paper, which has been published in Tectonophysics, is cited as Cossette et al. (2015) in the second article.

2. SEISMIC PROPERTIES AND MINERAL CRYSTALLOGRAPHIC PREFERRED ORIENTATIONS FROM EBSD DATA: RESULTS FROM A CRUSTAL-SCALE DETACHMENT SYSTEM, AEGEAN REGION

Élise Cossette[1], David Schneider[1], Pascal Audet[1], Bernhard Grasemann[2], Gerlinde Habler[3]
1. Department of Earth Sciences, University of Ottawa, Ottawa, Canada
2. Department of Geodynamics and Sedimentology, University of Vienna, Vienna, Austria
3. Department of Lithospheric Research, University of Vienna, Vienna, Austria

2.1 Abstract

The crystallographic preferred orientations (CPOs) were measured on a suite of samples representative of different structural depths along the West Cycladic Detachment System, Greece. Electron backscatter diffraction (EBSD) analyses were conducted on calcitic and mica schists, impure quartzites, and a blueschist, and the average seismic properties of the rocks were calculated with the Voigt-Reuss-Hill average of the single minerals' elastic stiffness tensor. The calcitic and quartzitic rocks have P- and S-wave velocity anisotropies (AVp, AVs) averaging 8.1% and 7.1%, respectively. The anisotropy increases with depth represented by the blueschist, with AVp averaging 20.3% and AVs averaging 14.5%, due to the content of aligned glaucophane and mica, which strongly control the seismic properties of the rocks. Localised anisotropies of very high magnitudes are caused by the presence of mica schists as they possess the strongest anisotropies, with values of ~25% for AVp and AVs. The direction of the fast and slow P-wave velocities occur parallel and perpendicular to the foliation, respectively, for most samples. The fast propagation has the same NE-SW orientation as the lithospheric stretching direction experienced in the Cyclades since the Late Oligocene. The maximum shear wave anisotropy is subhorizontal, similarly concordant with mineral alignment that developed during extension in the Aegean. Radial anisotropy in the Aegean mid-crust is strongly favoured to azimuthal anisotropy by our results.

Keywords: seismic anisotropy, crystallographic preferred orientation, Cyclades, fault zone
Word count: ~5900 main text; ~8300 all; **Tables:** 3; **Figures:** 6; **Appendix**: 1;
Supplementary material: 8 figures

2.2 Introduction

The Earth is often assumed to be isotropic for seismological modelling, yet most of our observations indicate that rock-forming materials do not conform to this model. Individual crystals in rocks have elastic properties that vary between their crystallographic directions thus creating seismic anisotropy, such that seismic velocities vary with the direction of propagation. Single crystals can be highly anisotropic with velocities varying by tens of percent along their different crystallographic axes. For example, P-wave velocities calculated for single crystals of olivine can differ by up to ~23% depending on the axes of propagation (cf. Nicolas and Christensen, 1987; Christensen, 2004). For olivine in the upper mantle, the anisotropy caused by alignment of these crystals during deformation is fundamental for the understanding of mantle flow (e.g. Babuska, 1972; Nicolas and Christensen, 1987 and references therein, Jung and Karato, 2001; Mainprice et al., 2005; Jung et al., 2014). In the crust, a crystallographic preferred orientation (CPO) in minerals can equally contribute to the observed seismic anisotropy (e.g. Lloyd et al., 2009, 2011; Dempsey et al., 2011, Bezacier et al., 2010; Ward et al., 2012). Muscovite is known to be highly anisotropic, with P- and S-wave velocities differing by up to 57% and 40%, respectively. In middle to lower crust, glaucophane anisotropy is not negligible, reaching 38% with P-wave velocities. With such anisotropic minerals, it is possible to calculate the seismic properties of a polycrystalline aggregate from textural (CPO) data (Mainprice 1990, 2011). The latter can therefore be used to infer the deformation features and metamorphic history of the rocks.

Whereas it is possible to study the deformation history of the crust via seismic anisotropy from textural data, we are interested in resolving their contribution to seismic velocity profiles. We sampled an exposed crustal-scale detachment zone exposed in the West Cyclades of Greece to obtain a theoretical vertical profile through this midcrustal structure, possessing a variety of lithotypes characterised by different seismic properties. Determining CPOs and calculating the elastic properties of the minerals and their aggregates are crucial in order to forward model wave propagation through the idealised vertical profile. The details gained from this experiment may therefore help to map rock composition and texture from velocity profiles. The Aegean region is well suited for such analyses due to its high

seismicity and to the exposure of fault networks. Moreover, studies of surface wave dispersion in this region likely point to seismic azimuthal and radial anisotropy caused by mineral alignment in the lower crust (Endrun et al., 2008, 2011). Here we present our results of mineral CPO determinations via electron backscatter diffraction (EBSD) analyses and bulk seismic properties of the various lithotypes across the exposed detachment. These results are part of a larger study, where we are building a seismic velocity model constrained by rock textures and seismic observations.

2.3 Geological setting

The Cyclades are part of the Aegean region, a back-arc basin formed during the south-south-westward retreat of the African slab, which is subducting below the southern margin of Eurasia (Jolivet and Brun, 2008). Extension in the region commenced in the Late Oligocene and resulted in the formation of metamorphic core complexes, exhumed along low angle normal faults (LANFs) through the Late Miocene (Jolivet et al., 2010). Individual LANFs exposed on the islands of Andros, Tinos and Mykonos define a single large-scale crustal detachment termed the North Cycladic Detachment System (Jolivet et al., 2010), and which records extension to the northeast. The West Cycladic Detachment System (WCDS, **Fig. 2-1**) is also a large-scale extensional structure that links detachments on several islands of the Cyclades (Kea, Kythnos, Serifos, Sifnos) and onto Lavrion in mainland Greece (Grasemann et al., 2012; Berger et al., 2013). The sense of shear is directed to the southwest, opposite of the North Cycladic Detachment System direction, defining symmetrical and bivergent extension of the Aegean region (Grasemann et al., 2012).

The Cyclades expose the Attic-Cycladic Crystalline Complex, which comprises two major units: the Cycladic Blueschist Unit and the Cycladic Upper Unit. These units are separated by LANFs and shear zones, consequently the Upper Unit commonly forms the hanging wall to the detachments. The Cycladic Blueschist Unit is composed of a poly-metamorphosed passive margin sequence (Dürr et al., 1978), and it structurally constitutes the footwall of Kea and Kythnos. These footwall rocks are mainly greenschist facies quartz- and calcite-bearing metapelites interlayered with mylonitic marbles (Iglseder et al., 2011; Grasemann et

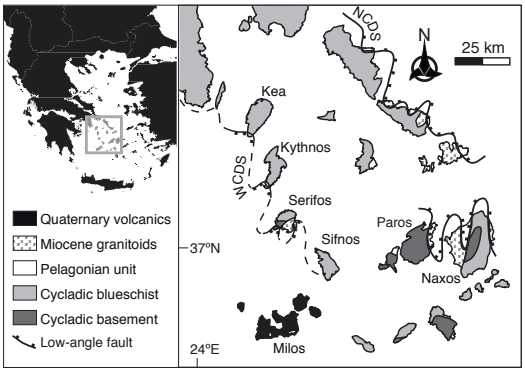

Figure 2-1. Simplified geological map of the Cycladic islands, showing location of the West Cycladic Detachment System (WCDS; simplified after Grasemann et al., 2012). Samples were taken from Kea, Kythnos and Sifnos, and the cross-section in Figure 2 is oriented ~NW-SE across these islands.

al., 2012). The LANF zones are up to 100 m thick, composed of footwall and hanging wall rocks exhibiting ductile to brittle deformation. On Kea and Kythnos, the detachment is mostly characterised by fine-grained ultramylonitic marbles with (proto-)cataclasites localised on the upper and lower contacts. Sheath folds in the marble ultramylonite on Kea indicate the detachment was a ductile high-strain zone (Grasemann et al., 2012). On Sifnos, an eclogite-blueschist unit is also present within the Cycladic Blueschist Unit together with marble and greenschist assemblages (Avigad, 1993).

The Cenozoic tectonics of the Western Cyclades involved at least two major events: (1) M1/D1 is a high-pressure/low-temperature metamorphic episode at 50-40 Ma (Schliestedt et al., 1987; Wijbrans et al., 1990; Tomaschek et al., 2003; Bröcker et al., 2004; Putlitz et al., 2005; Schneider et al., 2011) with a preserved ENE-WSW lineation in the Cycladic Blueschist Unit exposed on the islands (Schneider et al., 2011; Iglseder et al., 2011; Grasemann et al., 2012). These structures likely record extrusion from subduction to midcrustal conditions (Jolivet and Brun, 2008). (2) M2/D2 is characterised by a lower-amphibolite to greenschist-facies metamorphic overprint during the Miocene. Unroofing and cooling during crustal-scale extension occurred ca. 21-13 Ma, pervasively deforming the footwall greenschists and marbles, which record a top-to-SW-SSW displacement (Iglseder et al., 2011; Grasemann et al., 2012).

2.4 Analytical methods

Based on our previous work in the region (cf., Grasemann et al., 2012), we were able to strategically sample fault zone and/or footwall rocks from Kea, Kythnos, and Sifnos of the WCDS to reflect an idealised vertical profile of the detachment zone (**Fig. 2-2**). Rocks exhibiting clear foliation (preferred orientation of platy minerals and/or compositional layering) and lineation (fold axes, mineral or stretching lineation) structure and possessing micas were selected, in order to witness anisotropy in the rocks. We selected six rocks following petrographic analyses, targeting a range of lithotypes with unambiguous macroscopic structure, unaltered appearance, and simple mineralogy to favour good indexing during CPO analyses (indexed phases in **Fig. S1, S2**). Two samples (EC12-13 from Kythnos and EC12-11 from Kea) were taken in the LANF zone and represent the shallowest portion of the vertical profile. Two samples (EC12-09 and -12) are from the footwall on Kea and represent the middle portion of the vertical profile. Two samples (EC12-18 and -19) are from the footwall of the island of Sifnos and correspond to a deepest exposed portion of the crust along the WCDS.

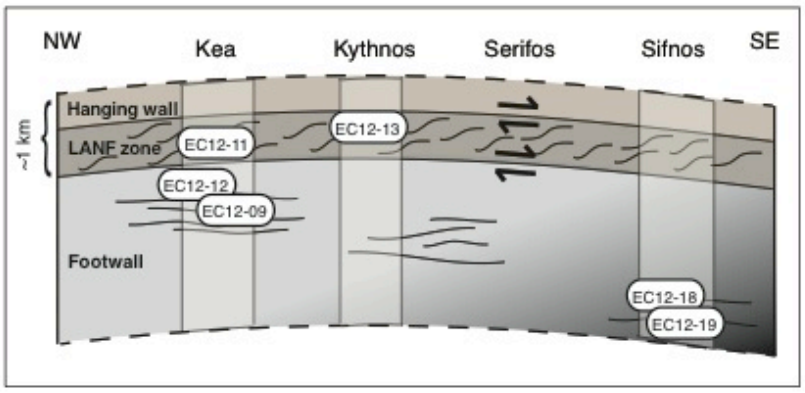

Figure 2-2. Simplified restored cross-section of the WCDS illustrating the theoretical structural depth of the sample locations across the shear zone.

All samples were cut into thin sections oriented parallel to lineation and perpendicular to foliation. In addition, a second set of thin sections was prepared parallel to lineation and at 30° to foliation for some samples (EC12-11, -13, -18), following the observation of Dempsey et al. (2011) that the percentage of indexing for micas was greater when cut at angles <45° to

foliation. Sample EC12-19 was cut differently because it exhibited cm-scale folding: the first section is perpendicular to the fold axis whereas the second section is parallel to the fold axis (**Fig. S3**). In both cases the section varies from parallel to perpendicular to foliation due to the fold structure.

The crystallographic orientations have been measured by EBSD analyses on a FEI Quanta 3D FEG instrument at the Department of Lithospheric Research (University of Vienna, Austria). The system is equipped with a field-emission electron source and an EDAX Pegasus Apex 4 system consisting of a Digiview IV EBSD camera and an Apollo XV Silicon Drift Detector for EDX-spectrometry. The EDAX OIM software V 6.2.1 was used for contemporaneous EBSD and EDX data collection. Samples were prepared as polished thin sections applying mechanical and final chemo-mechanical polishing. Colloidal silica suspension (pH 9.2-10) on a rotary polisher was used as polishing medium. Conductivity of the sample surface was secured with very thin carbon coating using a single carbon thread at vacuum conditions of $<10^{-5}$ mbar during evaporation. Measurements were taken at a working distance of 14 mm and a sample tilt of 70°. The beam conditions were set to 15 kV accelerating voltage and 2-4 nA beam current using spot size 1.0 in analytic mode and applying an SEM aperture of 1 mm. EBSD camera resolution was reduced using a 4 x 4 binning at an exposure time of 80-105 ms. In order to increase EBSD pattern contrast an intensity histogram normalisation filter and a dynamic background subtraction filter have been applied in addition to a static background subtraction filter. Hough settings of 1° theta step-size, a binned pattern size of 160 pixels, a 9 x 9 convolution mask and a minimum peak distance of 7-10 pixels were used for indexing 6-13 Hough peaks. The image quality parameter (IQ) maps are shown in **Fig. S4** and **S5**, and represent the average intensity of all detected Hough peaks. EBSD mapping was performed using beam scanning at step-sizes of 2-3.8 µm at indexing rates of 9-11 points per second. For most of the samples we obtained a number of scans from which we were able to measure CPO. Measurements for several minerals were acquired using OIM^{TM} Data Collection software, including muscovite, quartz, calcite, chlorite, albite, epidote and glaucophane. During data collection the Hough peaks and EDX data were stored, whereas later the scans were re-indexed based on the EDX signal intensities for specific elements ("Chemical assisted Indexing") and using up to 19 bands.

Data was cleaned up using OIM^{TM} Analysis for (1) grain CI (confidence index) standardisation using a minimum grain size of 2 mm and (2) neighbours orientation correlation (level 3, grain tolerance angle of 5°).

For sample EC12-12, the quartz phase has been reanalysed at the University of Western Ontario (London, Ontario), using a Hitachi SU6600 variable pressure, analytical field emission gun - scanning electron microscope (FEG-SEM; Schottky emitter). Methods follow Moser et al. (2011) and can be found in the **Appendix**. The EBSD data was then analysed using MTEX, a MATLAB^{TM} toolbox for textural analysis (Hielscher and Schaeben, 2008; Bachmann et al., 2010). Only data with a confidence index >0.1 have been used. Thin sections that are cut parallel to lineation and perpendicular to foliation have foliation in the xz plane, and the thin sections cut at 30° to foliation have the foliation in the plane y(z±60°) but were rotated to have the foliation in the xz plane as well. In order to compare the CPO data with the field observations, lineations measured in the field are denoted on a stereonet for each sample.

The CPOs have been characterised for every major mineral present in the thin section using pole figures from orientation density functions in MTEX. The EBSD dataset of mineral crystallographic orientations together with the elastic stiffness tensors of single crystals (references in **Table 2-1**) were the inputs to calculate the tensors of the mineral aggregates. These output tensors are given by the arithmetic mean of the Voigt and Reuss bounds (Voigt-Reuss-Hill average, Hill, 1952) and were thereafter used in the calculation of the samples' seismic properties. These physical properties (compressional and shear wave velocities and polarisation directions) were calculated by resolving the Christoffel equation (Mainprice et

Table 2-1. Elastic stiffness tensor values used in this study

Mineral	Density†	Elastic stiffness tensor (source)
albite	2.622	Brown et al. 2006
calcite	2.712	Chen et al. 2001
chlorite	2.800	Alexandrov & Ryzhova 1961
epidote	3.465	Aleksandrov et al. 1974
glaucophane	3.070	Bezacier et al. 2010
muscovite	2.834	Vaughan & Guggenheim 1986
olivine	3.311	Kumazawa & Anderson 1969
quartz	2.648	McSkimin et al. 1965

†g/cm3

al., 2011). Densities used in the calculation are derived from the mineral proportions noted during petrographic analyses. The formulas used for anisotropies are:

$$AVp = 200[(Vp_{max} - Vp_{min})/(Vp_{max} + Vp_{min})] \text{ and}$$

$$AVs = 200[(Vs1 - Vs2)/(Vs1 + Vs2)],$$

where Vs1 and Vs2 are the fast and slow S-wave velocities, respectively. AVp and AVs values are the P- and S-wave velocity anisotropies, respectively.

2.5 Results

Below we report sample descriptions, CPO results and seismic properties for the six samples. The modal proportions of minerals for the samples of this study are reported in **Table 2-2.** All pole figures are lower hemisphere equal area projections. Small pole figure insets show the plane of foliation and the lineations in each sample with the same reference frame as the EBSD maps. The pole figures for the thin sections cut 30° to foliation were rotated to show the same reference frame as the normal sections. Calculated velocities and anisotropies for all samples are listed in **Table 2-3**.

Table 2-2. Sample locations, mineral assemblages and structural measurements

sample	position	UTM 35 (N; E)	rock name	mineral assemblage† (vol %)							density	foliation	lineation
				Qz	Cal	Ms	Chl	Ab	Ep	Gn	(g/cm3)		
EC12-09	FW Kea	269996; 4171833	calcitic schist	**7**	**81**	**12**	-	-	-	-	2.7222	015/30	06-024
EC12-11	LANF Kea	266082; 4173978	calcitic schist	**17**	**50**	**18**	**4**	**11**	-	-	2.7167	356/11	14-039
EC12-12	FW Kea	268299; 4171153	mica schist	**45**	-	**50**	5	-	-	-	2.7486	251/32	18-039
EC12-13	LANF Kythnos	273592; 4136570	calcitic mylonite	**4**	**85**	**10**	-	**1**	-	-	2.7207	245/10	02-046
EC12-18	FW Sifnos	291217; 4099775	impure quartzite	**69**	-	**18**	-	-	**13**	-	3.0446	248/56	16-262 05-021 (cren.)
EC12-19	FW Sifnos	291228; 4099791	blueschist	**1**	**5**	**25**	7	2	25	**35**	3.0598	-	80-010 11-300 (fold)

† Bold values are the phases considered in the VRH average calculation of the elastic stiffness tensor

2.5.1 EC12-13: banded calcitic mylonite

Rock sample EC12-13 is a banded calcitic mylonite of the LANF zone on Kythnos. The matrix is composed of very fine-grained calcite that contains coarser quartz (0.1-0.2 mm), mica (0.2-0.5 mm long) and calcite (0.3 mm) crystals. Muscovite and quartz crystals are well dispersed in the matrix. Mica has a shape-preferred orientation with the basal planes subparallel to the orientation of the calcite twins, and some crystals have a micafish structure. Quartz grains are uncommon and isolated, and show undulose extinction. The

Table 2-3. Seismic velocities† and anisotropies calculated from the VRH averages

sample	scan*	Max Vp	Min Vp	Max Vs1	Min Vs1	Max Vs2	Min Vs2	**AVp %**	AVs1 %	AVs2 %	**Max AVs %**	Vp/Vs1 Max	Vp/Vs1 Min	Vp/Vs2 Max	Vp/Vs2 Min
EC12-9 calcitic schist	*norm scan01*	6.8834	6.2209	3.6561	3.4622	3.5615	3.3407	**10.1117**	5.4481	6.3982	**7.8430**	1.9321	1.742	1.9983	1.794
EC12-11 calcitic schist	30deg scan01	6.2402	5.9678	3.8921	3.7878	3.8229	3.7362	**4.4620**	2.7164	2.2926	**4.0283**	1.6336	1.5547	1.6604	1.5756
	30deg scan02	6.1795	5.9751	3.9032	3.8008	3.837	3.7663	**3.3641**	2.6584	1.8588	**2.9622**	1.6074	1.5558	1.6367	1.5654
	norm scan01	6.4858	5.8994	3.9059	3.6305	3.7924	3.5588	**9.4698**	7.3074	6.3557	**9.2239**	1.6684	1.569	1.8155	1.6021
	norm scan02	6.1820	5.8169	4.0346	3.8698	3.9197	3.8203	**6.0857**	4.1681	2.5671	**4.7245**	1.5495	1.4785	1.6156	1.5075
EC12-12 mica schist	*norm scan01*	6.9872	5.3447	4.3362	3.4381	3.8487	3.4085	**26.6383**	23.1043	12.1312	**23.8666**	1.6159	1.4572	2.0339	1.4972
EC12-13 calcitic mylonite	30deg scan01	6.7974	6.1971	3.6603	3.4767	3.4926	3.4025	**9.2392**	5.1445	2.6122	**6.5247**	1.879	1.7749	1.9596	1.8103
	30deg scan02	6.9221	6.0298	3.7713	3.428	3.5719	3.3521	**13.7790**	9.5385	6.3473	**11.0419**	1.8651	1.7323	2.0231	1.7773
	norm scan01	6.8369	6.1522	3.6652	3.4384	3.4753	3.3922	**10.5425**	6.3878	2.4195	**7.1659**	1.878	1.7785	1.9853	1.8121
EC12-18 impure quartzite	*30deg scan01*	5.9793	5.7550	3.9855	3.8572	3.9291	3.7684	**3.8222**	2.2725	4.1748	**4.7521**	1.5416	1.4449	1.5687	1.4918
	norm scan01	6.1473	5.5579	4.0788	3.6663	3.8103	3.5927	**10.0712**	10.6522	5.8786	**12.6347**	1.6199	1.435	1.6884	1.4778
EC12-19 blueschist	*para scan01*	7.2061	5.7345	4.0154	3.3978	3.6612	3.2506	**22.7443**	16.6615	11.8809	**18.6427**	1.9439	1.5562	2.1568	1.6579
	para scan02	7.8210	6.8948	4.3823	4.0517	4.2286	3.8806	**12.5877**	7.8399	8.5841	**10.9041**	1.86	1.6256	1.9302	1.6819
	perp scan01	8.4181	6.4581	4.6033	4.0215	4.4182	3.9203	**26.3509**	13.4918	11.9421	**14.5928**	1.8992	1.5049	2.1241	1.562
	perp scan02	7.5282	6.1821	4.2302	3.7695	4.009	3.6157	**19.6357**	11.5194	10.3169	**13.6987**	1.8022	1.5668	2.023	1.6472

† All velocities in km/s.

* Specifies if the section is cut normal (norm) or 30° (30deg) to foliation, and parallel (para) or perpendicular (perp) to fold axis. Representative figures in Fig.4 are from scans in italic.

coarser calcite crystals exhibit thin twins with a few (~20%) curved and tapered ones. This sample occupies the upper level of the vertical profile across the fault zone, and is the most deformed, defined by a mylonitic fabric.

Muscovite CPO is well defined with (001) parallel to foliation in all the scans, whereas [010] forms a girdle strongly aligned with the lineation (**Fig. 2-4 A1**), except in 30deg scan01 (**Fig. S6**). Calcite CPO is dominated by (0001) parallel to foliation, $[10\bar{1}1]$ and $[\bar{1}012]$ directions oriented along y and poles to $(\bar{2}021)$ forming a girdle along x (**Fig. 2-4 A2**). Quartz CPO has a weak texture defined by a [c] maxima at an angle along x in one scan (**Fig. 2-4 A3**) that could indicate prism [c] slip, and is well defined in 30deg scan02 that suggests basal <a> slip with [c] maxima in y directions (**Fig. S7**).

Vp_{max} in all the scans is parallel to lineation in the plane of foliation, and it varies between 6.80 and 6.92 km/s. Vp_{min} ranges between 6.03 and 6.20 km/s and is perpendicular to foliation. AVp_{max} and AVs vary between 9.2-13.8% (average: 11.2%) and 6.5-11.0%

(average: 8.2%), respectively. AVs_{max} occurs along the foliation and is mostly perpendicular to the lineation. The Vp/Vs ratio has its maximum parallel to lineation (**Fig. 2-4 A5, A6, A7**).

2.5.2 EC12-11: calcitic schist

Sample EC12-11 is from the detachment on Kea, and is a coherent calcitic schist. At the outcrop it is interlayered with mylonitic marbles. Micas define a weak S-C structure and are elongated (**Fig. 2-3 A, E**), with an aspect ratio between 12 and 20, and crystal lengths of 0.4-2.0 mm. Albite porphyroblasts are rotated to define sigma structures and strain shadows are often filled with recrystallised quartz or calcite. Quartz is small (0.05-0.1 mm) and exhibits undulatory extinction, subgrain rotation and bulging of grains. Calcite (0.25-1.0 mm) twins are thin or thick, and few are tapered.

Two thin sections of this schist were analysed via EBSD. The normal section shows a higher intensity of preferred orientation for the muscovite, compared to the 30° section (J-index of 9.3-14.2 versus 4.4-8.8 or maximum intensity of 12-15 versus 5.2-7.1 in **Fig. 2-4 B1 and S6**). In the four EBSD scans, (001) in muscovite is subparallel to foliation. Three scans (norm scan01-02 and 30deg scan01) show [010] in muscovite subparallel to the lineation and [0001] in calcite either in the y direction or forming a girdle symmetrically arranged along y (**Fig. 2-4 B1, B2, S6**). The other scan (30deg scan02) shows [010] in muscovite perpendicular to the lineation, but the quality of this dataset is poor (**Fig. 2-3 F**) and [0001] maximum in calcite parallel to the lineation (**Fig. S6**). Quartz CPO is obvious in the two scans: one is dominated by [c] in the z direction (**Fig. 2-4 B3**), inferring prism <a> slip, and the other one (norm scan02, **Fig. S6**) also displays [c] aligned in y directions and therefore combines prism and basal <a> slip. In chlorite (30deg scan02, **Fig. S6**), (001) is parallel to foliation, similar to the muscovite.

The calculated seismic properties for the two scans normal to foliation and the two scans 30° to foliation show Vp_{max} in the plane of foliation and parallel to lineation, varying between 6.17 and 6.48 km/s. Vp_{min} is perpendicular to foliation and varies between 5.82 and 5.98 km/s. AVs_{max} appears to be higher in the normal sections (4.7-9.2%) than in the 30° sections (3.0-4.0%). The same is observed for AVp, where it is 6.1-9.5% in normal sections and 3.4-

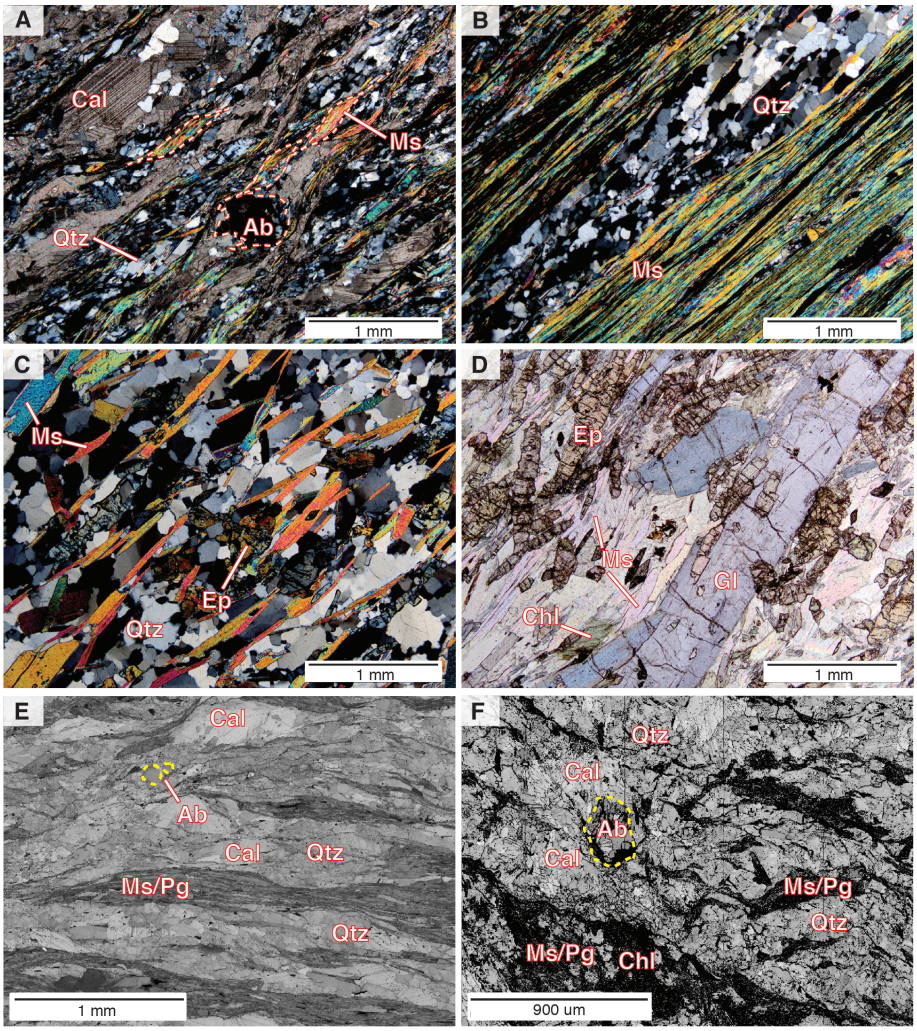

Figure 2-3. A-D: Crossed-polar photomicrographs (except D in plane light) from 30μm thick thin sections of the samples. A: calcitic schist EC12-11, B: mica schist EC12-12, C: impure quartzite EC12-18, D: blueschist EC12-19. E-F: Image quality (IQ) maps describing the quality of an electron backscatter diffraction pattern. Darker gray shades in the image denote lower IQ values. E: sample EC12-11 norm scan01, F: sample EC12-11 30deg scan02. Abbreviations are as follows: Ab: albite, Cal: calcite, Chl: chlorite, Ep: epidote, Gl: glaucophane, Ms: muscovite, Pg: paragonite, Qz: quartz.

4.5% in 30° sections. AVs_{max} occurs subparallel to lineation, and the Vp/Vs ratio is also higher parallel to lineation (**Fig. 2-4 B5, B6, B7**).

2.5.3 EC12-12: mica schist

The mica schist sample EC12-12 is from the footwall of Kea, and exhibits a macroscopic S-C structure. The aspect ratio of the muscovite is large (10 to 30), and the layers of mica

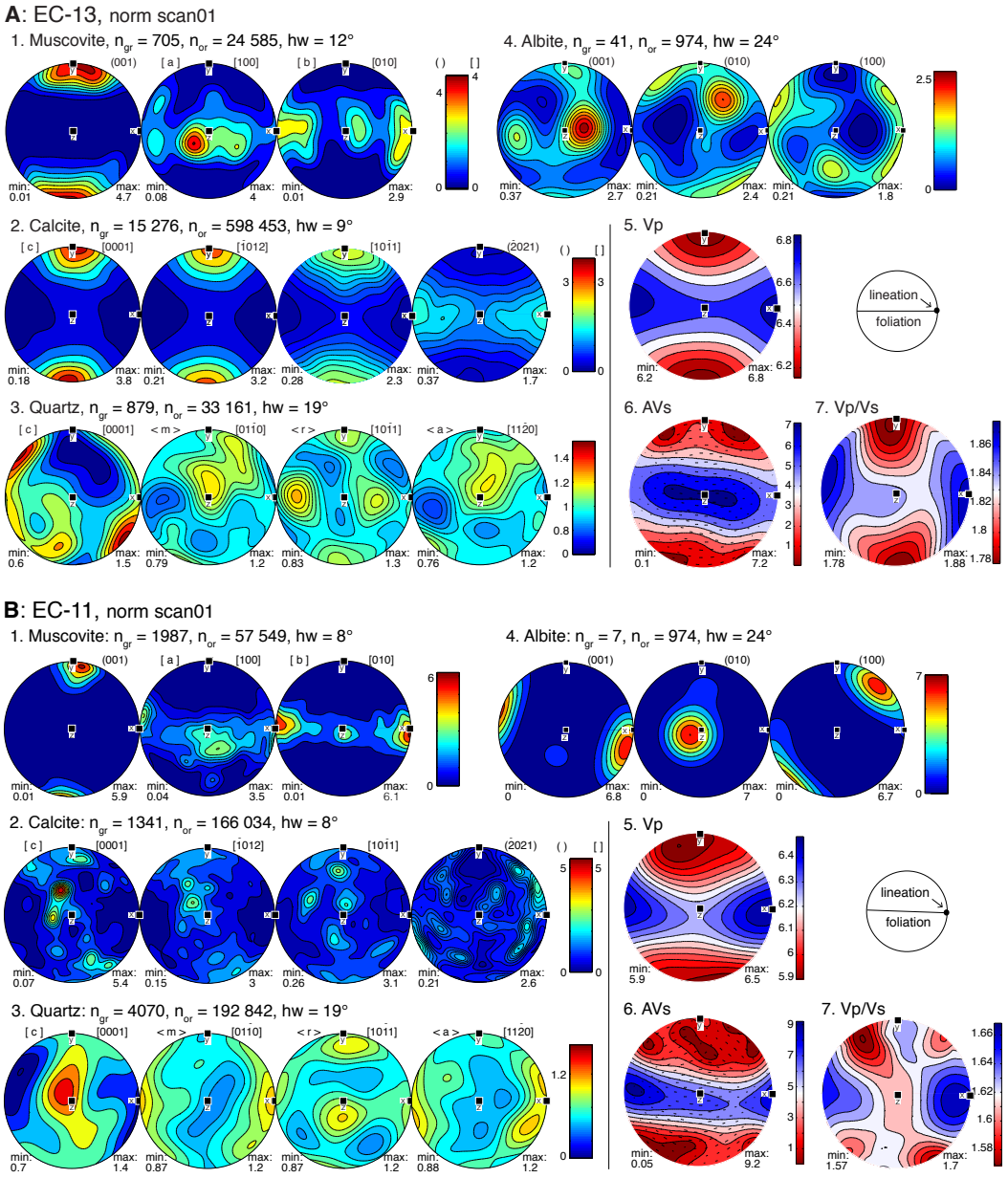

Figure 2-4. A-F: For each sample, representative pole figures showing mineral CPOs and seismic figures illustrating P-wave velocity orientation, S-wave velocity anisotropy with Vs1 polarisation directions and Vp/Vs ratio. Pole figures show the density distribution of plane poles/crystallographic directions as equal-area, lower hemisphere projections. Small pole figure insets show the plane of foliation and the lineation for each sample. n_{gr} and n_{or} are the number of grains and orientations used in the density calculation, respectively, and hw is the half-width used in the pole figures.

alternate with ribbons of recrystallised quartz (0.02-0.1 mm, **Fig. 2-3 B**). Dynamic recrystallisation is indicated in quartz by subgrain rotation, indented bulging of grains and undulatory extinction.

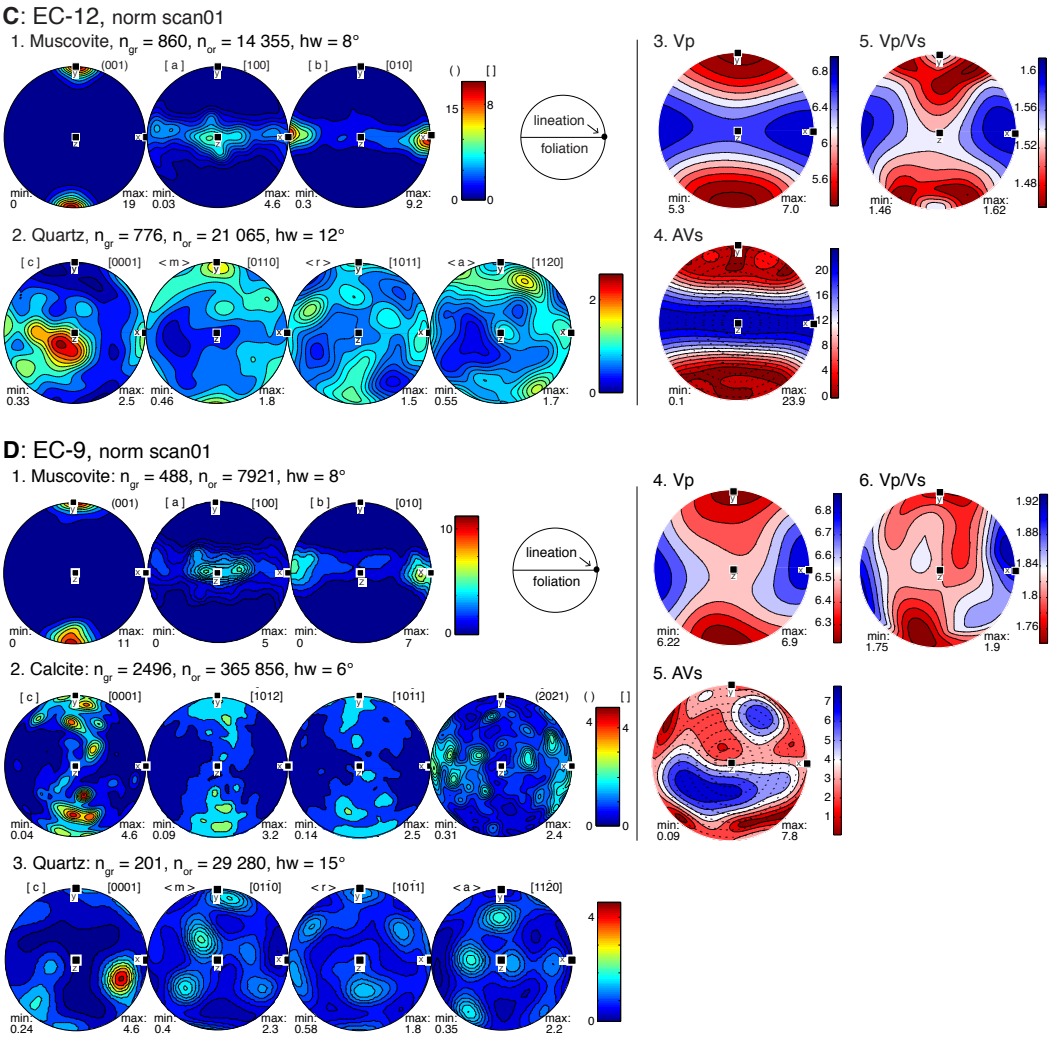

Figure 2-4 (continued). A-F: For each sample, representative pole figures showing mineral CPOs and seismic figures illustrating P-wave velocity orientation, S-wave velocity anisotropy with Vs1 polarisation directions and Vp/Vs ratio. Pole figures show the density distribution of plane poles/crystallographic directions as equal-area, lower hemisphere projections. Small pole figure insets show the plane of foliation and the lineation for each sample. n_{gr} and n_{or} are the number of grains and orientations used in the density calculation, respectively, and hw is the half-width used in the pole figures.

Only one thin section normal to foliation was analysed via EBSD for this sample. Mica CPO (**Fig. 2-4 C1**) is very strong with (001) parallel to foliation and [010] parallel to lineation. Quartz has also a strong CPO with [c] in the z direction, implying prism <a> slip (**Fig. 2-4 C2**).

This sample possesses the highest anisotropy (AVs_{max} is 23.9% and AVp is 26.6%) in our suite of rocks. Vp_{max} is 6.99 km/s and occurs in the plane of foliation, parallel to lineation,

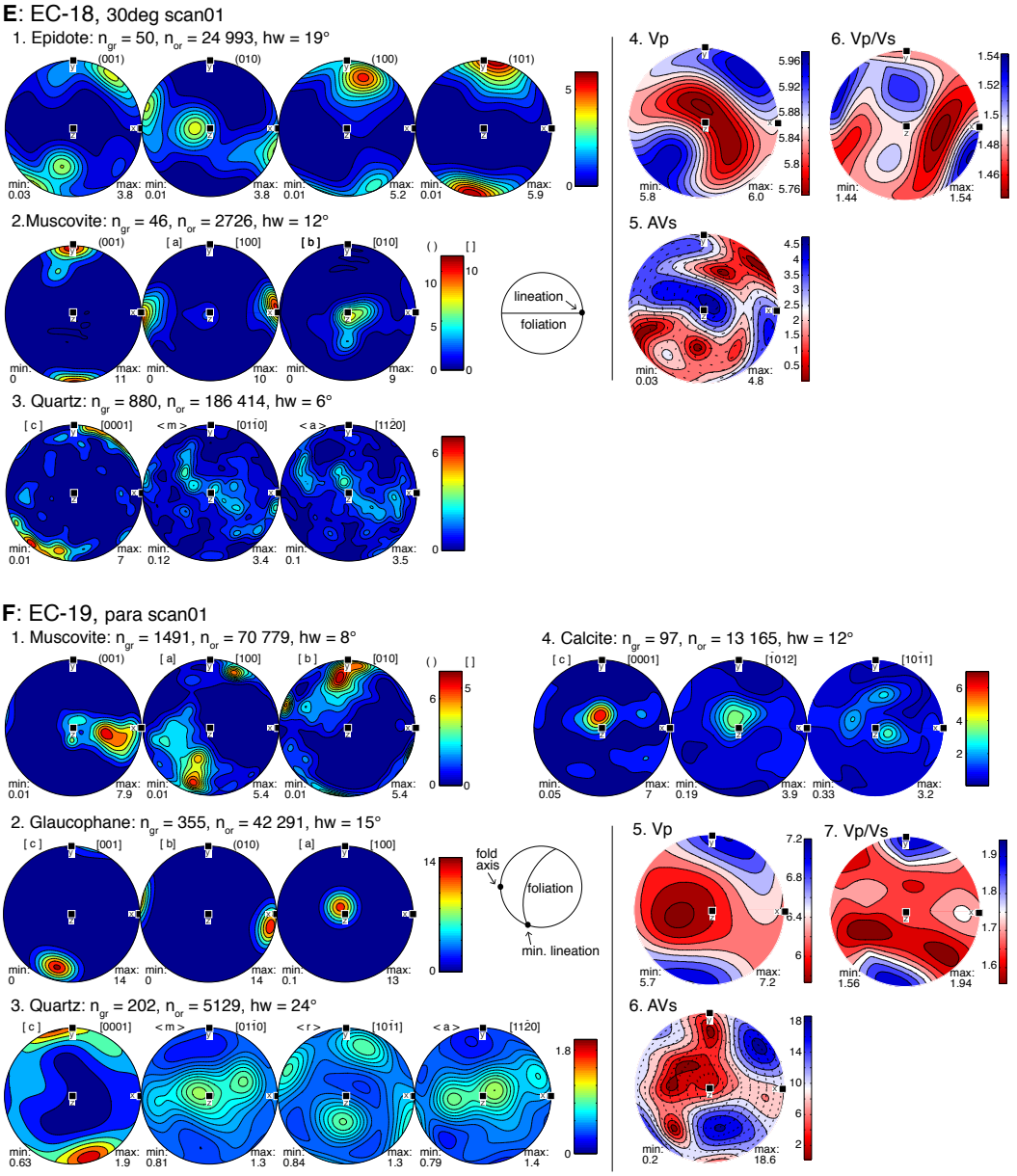

Figure 2-4 (continued). A-F: For each sample, representative pole figures showing mineral CPOs and seismic figures illustrating P-wave velocity orientation, S-wave velocity anisotropy with Vs1 polarisation directions and Vp/Vs ratio. Pole figures show the density distribution of plane poles/crystallographic directions as equal-area, lower hemisphere projections. Small pole figure insets show the plane of foliation and the lineation for each sample. n_{gr} and n_{or} are the number of grains and orientations used in the density calculation, respectively, and hw is the half-width used in the pole figures.

and Vp_{min} is 5.34 km/s and is found perpendicular to foliation. AVs_{max} and the highest Vp/Vs ratio are also in the plane of foliation and parallel to lineation (**Fig. 2-4 C3, C4, C5**).

2.5.4 EC12-9: calcitic schist

From the footwall of Kea, sample EC12-09 is a calcitic schist and was sampled from a dark grey marble outcrop interlayered with brown-coloured schists. In thin section, subgrain rotation and low-temperature bulging of grains indicate recrystallised quartz. Some quartz grains exhibit sigma structures with recrystallised subgrains. Elongated white mica defines the foliation in the calcite matrix, with aspect ratios (length/width) between 10 and 20 and crystal lengths of 0.4-1.0 mm. Calcite (0.15-1.0 mm) is a little altered and it is deformed, exhibiting a variety of tabular thin, thick and tapered twins.

Results of the EBSD analyses demonstrate that the muscovite has a strong preferred orientation with the plane (001) parallel to foliation, the crystallographic direction [010] parallel to lineation, and the direction [100] weakly oriented perpendicular to lineation and in the plane of foliation (**Fig. 2-4 D1**). Calcite has a weak preferred orientation with [0001] forming a crossed girdle along y, and [$\bar{2}$021] slightly arranged symmetrically along x (**Fig. 2-4 D2**). The quartz CPO is dominated by a [c] maximum in the x direction, although a bit off centre, possibly implying prism c-slip (**Fig. 2-4 D3**).

The phases considered in the calculation of the Voigt-Reuss-Hill average are muscovite, quartz and calcite. The maximum P-wave velocity (Vp_{max}, 6.88 km/s) is in the same direction as the lineation, in the plane of foliation, whereas the minimum P-wave velocity (Vp_{min}, 6.22 km/s) is perpendicular to foliation. The maximum shear wave anisotropy (AVs_{max}) and the compressional wave anisotropy (AVp) are 7.8% and 10.1%, respectively. The Vp/Vs ratio is higher parallel to lineation, and AVs_{max} is at ~10 to 40° to the plane of foliation (**Fig. 2-4 D4, D5, D6**).

2.5.5 EC12-18: impure quartzite

Two rock specimens from Sifnos island correspond to deeper levels in the footwall. EC12-18 is an impure quartzite with a beige-pink colour and crenulation cleavage. Mica crystals are not strained; they are rather prismatic and equant (**Fig. 2-3 C**), and a few exhibit kink bands. Their aspect ratio is between 2.5 and 10 and crystal lengths vary between 0.3 and 0.8 mm. Some crystals crosscut the main foliation at ~35°. Quartz (0.1-0.6 mm) shows fractures,

subgrain rotation and grain bulging with indentations. Epidote has a poikilitic texture with quartz inclusions.

Muscovite CPO determined by EBSD analysis is controlled by (001) parallel to foliation. Norm scan01 (**Fig. S7**) exhibits [010] parallel to lineation while 30deg scan01 (**Fig. 2-4 E1**) exhibits [010] perpendicular and [100] parallel to lineation. The (100) plane of paragonite in the pole figure from norm scan01 is parallel to foliation whereas in the 30deg scan01 pole figure (**Fig. 2-4 E4**) it is inclined ~40° to foliation. In this latter scan, however, the indexing for paragonite was very poor (**Fig. S2**). The quartz orientations are indicative of basal <a> slip with the [c] maxima close to the y directions and <a> forming a girdle along xz (**Fig. 2-4 E3**). The quartz pattern in the norm scan01 pole figure suggests prism <a> slip with [c] maxima in the z direction, although the maxima is off centre. Epidote pattern displays (101) subparallel to foliation and a girdle of [010] along x in 30deg scan01 (**Fig. 2-4 E3**).

Vp_{max} in the normal section (6.14 km/s) is in the plane of foliation, oriented about 30° from the lineation, and Vp_{min} (5.56 km/s) is perpendicular to foliation. The maximum S-wave anisotropy (13.0%) occurs parallel and also perpendicular to lineation along foliation, and the P-wave anisotropy is 10.1%. The scan from the 30° section shows a Vp_{max} with a weak relation to the main foliation; however it seems related to the paragonite, quartz and epidote CPOs (**Fig. 2-4 E5, E6, E7**). Vp_{max} (6.0 km/s) is oriented ~40° to the lineation, not in the plane of foliation and Vp_{min} (5.76 km/s) is subparallel to (001) in paragonite and to (101) in epidote. AVs is 4.8% and AVp is 3.8%; averages of AVp and AVs are 6.9 and 8.7%, respectively.

2.5.6 EC12-19: blueschist

The blueschist sample EC12-19 is folded on the cm-scale and has a complex foliation (due to folding) defined mostly by glaucophane, and to a lesser extent by muscovite. Glaucophane crystals have an aspect ratio of 3-10 and can be as long as >1 cm. Mica is much smaller, with an aspect ratio of 2-10 and crystal lengths of 0.3-1.5 mm (**Fig. 2-3 D**). The rock has an abundance of prismatic and fractured epidote, and a few pseudomorphs of chlorite after garnet.

The thin sections for this sample were taken through and across a fold and therefore the plane of foliation is not the same for all EBSD scans. However, it is possible to relate planes of foliation with the mineral CPOs by examining the EBSD maps and the thin sections. A sketch of the fold with the foliation and lineation orientations is provided in the supplementary material (**Fig. S3**). Glaucophane consistently has the (010) plane parallel or subparallel to foliation, and the [001] crystallographic direction in the plane of foliation and parallel to the mineral lineation (**Fig. 2-4 F2**). Muscovite is dominated by (001) subparallel to foliation and [010] parallel to mineral lineation (**Fig. 2-4 F1**). Calcite CPO is not consistent among the scans. It has [0001] in the plane of foliation perpendicular to the mineral lineation in para scan01 (**Fig. 2-4 F4**), but [0001] parallel to the lineation in para scan02 (**Fig. S7**). The scans perp scan01 and -02 have [0001] in calcite perpendicular to subperpendicular to foliation (**Fig. S7**). Quartz CPO possibly implies prism c-slip during deformation as indicated by [c] roughly along y and <a> girdle across the x direction (**Fig. 2-4 F3**).

The maximum P-wave velocity is strongly correlated with the CPOs of muscovite and glaucophane (**Fig. 2-4 F1, F2, F5**). It varies from 7.21 to 8.42 km/s between the four scans and it is parallel to the lineation and in the plane of foliation, whereas the slowest P-wave velocity (5.73-6.89 km/s) is perpendicular to foliation (**Fig. 2-4 F**). AVs maximum varies from 10.9 to 18.6% (average: 14.5%), and AVp varies from 12.6 to 26.4% (average: 20.3%). The Vp/Vs ratio is higher parallel to lineation (**Fig. 2-4 F7**).

2.6 Discussion

2.6.1 Accuracy of the calculated data

The consistency of the observed CPOs between the different scans of single samples is supposed to be an important criterion for considering CPOs to be accurate. Although the thin section areas for the scans were chosen on the basis of being representative of the whole rock, some samples show dissimilarities between different scans of single samples, indicating that care must be taken when interpreting the data. Muscovite and glaucophane exhibit the same crystallographic preferred orientation systematics in different scans of the

same sample EC12-19, thus suggesting reproducibility of the data. The scans perp scan01 and para scan02 exhibit coarse-grained glaucophane and these single grains could dominate the density distribution since all orientations are considered in the density calculation. However, the results are still similar to the other scans where glaucophane grains are smaller. It must be stated that diverse CPOs and therefore different slip systems for quartz were observed among different scans of the same sample, possibly suggesting their co-existence at a very small scale. The last metamorphic episode (M2), that occurred under greenschist to lower amphibolite facies in the Aegean, would likely lead to basal or prism <a> slip deformation (i.e. low-medium temperature deformation) in quartz. Prism [c] slip becomes important above 650°C (e.g. Mainprice et al., 1986) and is thus not likely expected in our samples, which only experienced temperatures of 280-400°C during M2 (Iglseder et al., 2011). Different CPOs were observed for albite as well, even in the same thin section, and therefore the CPO is less conclusive. In this case, only a few small albite grains were analysed in different scans of EC12-11, and these datasets are probably not sufficiently large to obtain a CPO – the texture is then controlled by single grain orientations. Otherwise, since the temperatures reached during the greenschist deformation of the footwall were low, albite porphyroblasts possibly did not undergo plastic deformation, which commonly starts around 400-500°C (Fitz Gerald and Stünitz, 1993 and references therein).

The quality of the diffraction patterns is variable among the scans of a sample (e.g. **Fig. 2-3 E-F**). It appears that this difference in image quality (IQ) is sometimes related to the cut of the section, with the normal sections exhibiting better IQ maps (**Fig. S5, S5**). The only other distinction observed between the sections cut normal and 30° to foliation is in sample EC12-11, where the intensity of CPO is lower in the 30° sections. Since it is not apparent in other samples, this might not be related to the plane of section. For these reasons and since pole figures derived from data of 30° sections are less straightforward and necessitate more treatment (i.e. rotations) it is reasonably more appropriate to study normal-cut sections.

2.6.2 CPO control on the average seismic properties

Overall, the maximum P-wave velocities in the rocks are found along foliation planes and parallel to lineation, the minimum P-wave velocities are found perpendicular to foliation

planes, and the maximum S-wave anisotropy occurs along foliation. This strongly suggests that the mineral CPOs regulate the P- and S-wave behaviour, which is consistent with several other EBSD studies (e.g. Bascou et al., 2000; Lloyd et al., 2009; Bezacier et al., 2010; Brownlee et al., 2011; Cao et al., 2013; Erdman et al., 2013; Ji et al., 2013). Transverse isotropy is consequently a good approximation for AVp, where the axis of symmetry represents the slow axis of wave propagation, perpendicular to foliation. It is a good estimation for AVs as well, with the minimum splitting between Vs1 and Vs2 oriented perpendicular to foliation. Samples EC12-18 and -19, however, show a Vp minimum almost in the plane of foliation and a heterogeneous pattern of AVs.

In the case of EC12-18, the seismic properties appear to correspond to the CPOs of quartz and epidote (**Fig. 2-4 E**). Despite the similarity with epidote pattern, it is still unusual to obtain the Vp maximum sub-perpendicular to foliation, because epidote commonly aligns its seismically fast plane with the plane of foliation (e.g. Bezacier et al., 2010, Daeyeong et al., 2013). EC12-18 has a particularly high concentration in quartz and therefore the resulting seismic anisotropy may imply an interference with quartz. Such interferences have been documented by Ward et al. (2012) between quartz and mica: in their study, the maximum Vp pattern is increasingly controlled by the active quartz slip system at high quartz:mica ratios, such that at low quartz:mica ratio, the mica CPO controls the Vp pattern. According to their synthetic orientation data, an active basal <a> slip system in quartz (such as in **Fig. 2-4 E3**) with a quartz:mica ratio of >9 induces minimum velocities along foliation, but the shift seems to appear at a ratio of 4. The quartz:mica ratio in EC12-18 has a value around 3.8 (muscovite and paragonite added together). This could, in part, explain why Vp maximum occurs almost perpendicular to foliation in EC12-18.

In glaucophane, the seismically fast direction is along the c-axis, and in muscovite, it is along the a- and b-axes (**Fig. S8**). The orientation of these two minerals' axes in EC12-19 ensures that Vp maximum is coincident with a single orientation (along the y axis in **Fig. 2-4 F5**, which is along foliation). This constructive relationship has the effect of increasing AVp up to 19%. The seismically slow directions in glaucophane and muscovite are the a- and c-axes, respectively, implying that glaucophane has the main control on the resulting average Vp

minimum, which occurs almost in the plane of foliation, but still perpendicular to Vp maximum (**Fig. 2-4 F2, F5**). Sample EC12-19 contains a certain concentration in epidote and chlorite, which were not measured via EBSD methods and could not be accounted for in the seismic property calculations. Yet these two minerals may have quite high anisotropies: in epidote, AVp: 26.3% and AVs: 35.3% (Bezacier et al., 2010) and in chlorite, AVp: 35% and AVs: 76% (Mainprice and Ildefonse, 2009). The 25 vol.% of epidote in EC12-19 surely has an effect on the resulting anisotropy, although since the epidote fast plane aligns with foliation together with glaucophane, the seismic anisotropy remains high, as has been observed by Bezacier et al. (2010) and Fujimoto et al. (2010). Moreover, the high concentration in epidote is not widespread in the Sifnos blueschists, which commonly possess <20% of epidote (Altherr et al., 1979; Schliestedt and Matthews, 1987; Wijbrans et al., 1990; Ring et al., 2011). To account for the chlorite anisotropy, a sensitivity test was conducted using the chlorite CPO of sample EC12-11 for the seismic anisotropy calculation of sample EC12-19. The chlorite has been oriented with the same orientation as the muscovite. Using para scan01, adding 7% chlorite increased AVp of 0.3% and decreased AVs of 1.7%. We can be fairly confident that adding epidote and chlorite in the calculation, if they have well defined CPO, would still give higher anisotropies than the ones obtained in the calcitic schists.

2.6.3 Seismic anisotropy in the Cycladic mid-crust

Our results show that the rocks possessing the highest anisotropy are the mica schist (AVp_{max}: 26.6%, AVs_{max}: 23.9%) and the blueschist (AVp_{max}: 26.35%, AVs_{max}: 14.59%). The rest of the samples (calcitic and quartzitic rocks) have AVp varying between 3.4% and 13.8% (average: 8.1%), and AVs varying between 3.0% and 12.6% (average: 7.1%). Consequently, we do not observe a positive correlation between anisotropy and the localisation of deformation in the vertical profile (**Fig. 2-5**). In fact, the fault zone is apparently not the most anisotropic. There is however a pronounced increase in overall anisotropy deeper in the footwall, as illustrated by the blueschist. The mica schist also possesses strong anisotropies of 24-27%.

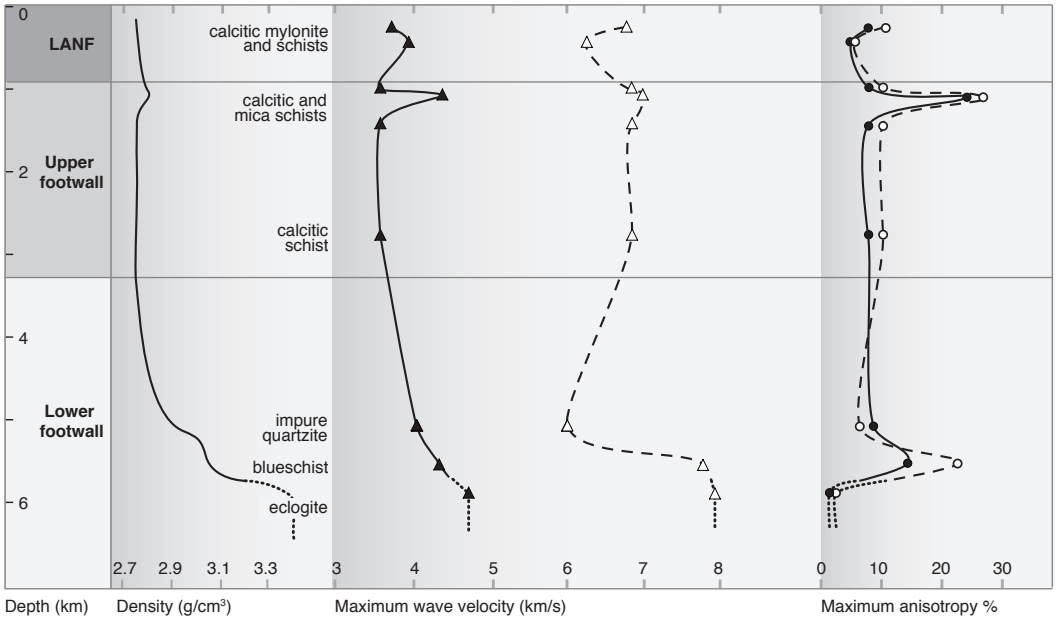

Figure 2-5. Seismic wave velocity (triangles) and anisotropy (circles) profile with respect to structural position. Shallow depths are at the top of the diagram and the scale is highly approximate. On the velocity and anisotropy profiles, solid black line represents data for the S-wave and dashed line is for the P-wave. Dotted line represents values calculated for glaucophane bearing eclogite from Bezacier et al. (2010) with a density of 3.45 g/cm3.

The mineralogy is thus the main control for the observed anisotropy distribution, and higher anisotropy magnitudes are obtained from mica-rich and glaucophane-rich rocks since these minerals develop a well defined crystallographic preferred orientation. This was predictable, as mica has been documented as the most anisotropic mineral in the upper-middle crust, and amphibole being suggested as the principal contributor to seismic anisotropy in the deep crust (e.g. Ward et al., 2012; Tatham et al., 2008; Ji et al., 2013). Thus the crust likely contains, on a vertical profile, several sections of high anisotropies due to mica schists interlayered with other lithotype. Other studies on seismic anisotropy (e.g. Meltzer and Christensen, 2001; Erdman et al., 2013) have reported averages of AVp of 7% and AVs of 9-12% in quartzofeldspathic gneisses and calc-silicate rocks, with the highest anisotropies determined from micaceous samples. In our study, the seismic anisotropy generally increases with samples that are more representative of deeper structural levels, which is the blueschist component of the Lower Unit in the Attic-Cycladic Crystalline complex. At these lower depths, conversely, the eclogite component of the crust would likely decrease the seismic anisotropy; Bezacier et al. (2010) determined that eclogites from the Western Alps had an

AVp of 2.9% and AVs of 1.7% (**Fig. 2-5**). Understandably, the number of different phases and their abundance also strongly influence the whole rock anisotropy that we have calculated. Samples EC12-9, -11 and -13, which have high concentration of calcite, possess somewhat low S-wave anisotropies varying between 3% and 11%. Sample EC12-18, which probably demonstrates destructive interference between mica and quartz, also has an epidote phase, and possesses the lowest S-wave anisotropy in the samples, at 4.7-6.4%.

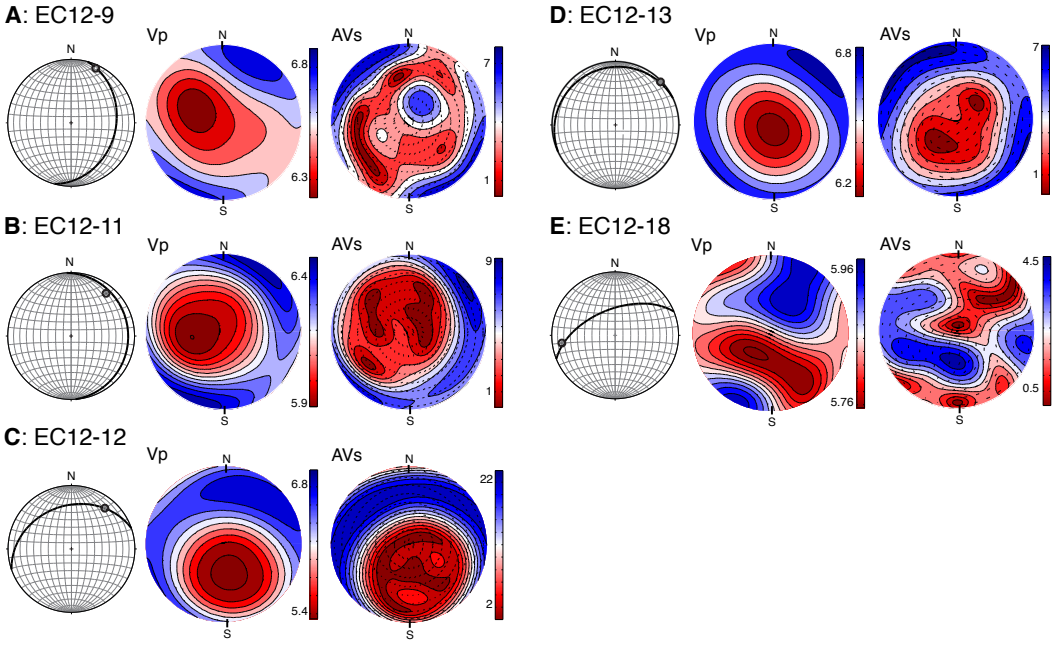

Figure 2-6. P-wave velocities and S-wave velocity anisotropies geographically oriented, using field structural measurements (plane of foliation and lineation on small stereonet). Data plotted on equal-area, lower hemisphere stereonets. Data for EC12-19 (blueschist) not shown since the sample was of a cm-scale fold. Samples exhibit a subvertical slow axis of wave propagation.

The direction of the maximum P-wave velocities correlates very well with the lineations observed in the field (**Fig. 2-6**). On the islands of Kea, Kythnos, and Sifnos, Vp_{max} is plunging northeast or southwest and can be directly related to the direction of Miocene extension in the Cyclades, indicated by N-NE or S-SW stretching lineations (e.g. Walcott and White, 1998; Trotet et al., 2001; Iglseder et al., 2011; Ring et al., 2011; Grasemann et al., 2012). Endrun et al. (2011) also documented strong azimuthal anisotropy in the lower crust with NE-SW fast-propagation directions. The orientation of the maximum compressional and shear wave velocity anisotropy for the samples in this study is

subhorizontal (**Fig. 2-6**), which is concordant with the Aegean lithospheric extension and the consequent horizontal alignment of minerals in the crust. The maximum Vp and AVs are gently plunging due to the shape of the metamorphic domes. Our results strongly support that mineral alignment in the lower crust is the likely cause for radial anisotropy in the Aegean, as noted by Endrun et al. (2008). Our data further suggest that radial anisotropy is much greater than azimuthal anisotropy, since the symmetry axis (the slow axis of wave propagation) is subvertical (**Fig. 2-6**).

The high shear wave anisotropy found in the mica schist and in the blueschist indicates that these rock units are good candidates for generating shear wave splitting. Our data illustrate that the greatest S-wave splitting occurs principally along the foliation. This means that for normally-incident waves, splitting could be detected only for dipping rocks. Due to their domal structure, most of the islands in the Cyclades exhibit gently dipping rock units (**Table 1-1**). A strong shear wave splitting could also allow the detection of such mica schists and blueschists at depth, in the upper-middle crust.

2.7 Conclusion

- The calcitic and quartzitic rocks have P- and S-wave velocity anisotropies (AVp, AVs) averaging 8.1% and 7.1%, respectively. The blueschist possesses an AVp averaging 20.3% and an AVs averaging 14.5%. The mica schist has values of 26.6% and 23.9% for AVp and AVs, respectively.
- The crystallographic preferred orientation of the constituent minerals in a rock has a control on the average seismic anisotropy. Muscovite and glaucophane develop a particularly strong CPO and have seismic properties that are constructive.
- AVs and AVp both show transverse isotropy. Fast and slow velocities of P-waves occur along the foliation and across the foliation, respectively, due to the content of aligned mica and amphibole.
- The maximum seismic anisotropies are found in mica schist and blueschist rocks. On a suite of samples that represent different structural depths across the West Cycladic shear zone, the anisotropy increases with depth because of the blueschist component

in the Cycladic Blueschist Unit. Localised high anisotropies are due to micaceous rocks.

- Fast velocities of P-waves are in the same orientation (NE-SW) as the displacement direction of extension that is occurring in the Aegean due to the slab retreat. The maximum S-wave velocity anisotropy is subhorizontal for all samples of the Cyclades, parallel with mineral alignment developed during lithospheric extension, suggesting strong radial anisotropy.

2.8 Appendix: EBSD methods for quartz phase in EC12-12

Electron beam images and analyses were collected with a Hitachi SU6600 variable pressure, analytical field emission gun - scanning electron microscope (FEG-SEM; Schottky emitter) located in the Zircon and Accessory Phase Laboratory at the University of Western Ontario, London, Ontario, Canada. Backscatter electron (BSE) imaging was carried out with a five segment solid-state detector utilizing a low accelerating voltage (5kV) to stimulate channelling contrast effects and highlight structural variations within the crystals. Colour CL images of visible and ultraviolet light were collected with a customized Gatan ChromaCL detector system and Gatan DigitalMicrograph software using a 10 kV electron beam. Microstructural data were collected with an Oxford Instruments Nordlys EBSD detector. The epoxy mount containing the rock samples was tilted to 708 within the SEM chamber and raised to a working distance of 19.0 mm. A 20 kV, 8.0 nA electron beam was used to generate EBSD "maps" consisting of an orthogonal grid of electron backscatter diffraction patterns (EBSPs) acquired at 55 frames/s at step sizes ranging from 50 to 600 nm using EBSD software (Oxford HKL Channel 5). EBSD camera settings included 4 x 4 binning, high gain, a frame averaging of 7, and a combined static and dynamic background removal routine. Empirically obtained EBSPs were indexed using a minimum of five and a maximum of seven Kikuchi bands, using a Hough transform resolution setting of 60. The mean angular deviation (MAD) discriminator of the obtained EBSP was set to a value of 1.78, above which analyses were assigned a zero solution to avoid indexing of poor quality EBSPs. Post-analysis noise reduction processing was not applied to any of the data sets. Elemental identification and mapping were conducted by X-ray energy dispersive spectrometry (EDS)

using an Oxford Instruments X-Max 80 mm^2 silicon drift detector and processed with INCA Energy software.

3. STRUCTURE AND ANISOTROPY OF THE CRUST IN THE CYCLADES (GREECE) USING RECEIVER FUNCTIONS CONSTRAINED BY IN SITU ROCK TEXTURAL DATA

Élise Cossette[1], Pascal Audet[1], David Schneider[1], Bernhard Grasemann[2]
1. Department of Earth Sciences, University of Ottawa, Ottawa, Canada
2. Department of Geodynamics and Sedimentology, University of Vienna, Vienna, Austria

3.1 Abstract

Seismic velocity models are often used to constrain rock composition and textures in the crust based on compilations of rock properties that may not be representative of the local geology. In this paper we use teleseismic receiver functions jointly with in situ rock property data to constrain the seismic structure and anisotropy of the crust in the Cyclades (Greece), located in the back arc region of the Hellenic subduction zone. The receiver function data indicate that the Moho is relatively flat at 25 km depth toward the south and deepens to 33 km in the north, consistent with previous studies, and reveal an intra-crustal discontinuity varying from 3 to 11 km, mostly observed in the south-central Aegean. Harmonic decomposition of the receiver functions further indicates the presence of both shallow and deep crustal anisotropy related to crustal structures. We model synthetic receiver functions based on constraints from in situ rock properties that we recently measured using the electron-backscatter diffraction technique. Our results indicate that the shallow upper crustal layer is characterized by metapelites with ~5% anisotropy, underlain by a 20 km thick and possibly anisotropic layer of high-pressure rocks comprising blueschist and eclogite and/or restitic material from Miocene magmatism. This study demonstrates the importance of rock textural constraints in the interpretation of seismic velocity profiles.

Keywords: seismic anisotropy, receiver functions, numerical modelling
Word count: ~6300 main text; ~8000 all; **Tables:** 2; **Figures:** 6

3.2 Introduction

Seismic anisotropy (the variations of seismic wave propagation with direction) is a powerful tool to study the alignment of minerals in the crust and mantle resulting from large-scale,

coherent deformation caused by tectonic processes (e.g. Jolivet et al., 2009; Porter et al, 2011; Endrun et al., 2011). In the upper mantle, seismic anisotropy is generally interpreted as arising from past or current tectonic processes leading to flow-induced crystallographic preferred orientation of dry olivine (e.g. Nicolas and Christensen, 1987; Ben Ismaïl and Mainprice, 1998; Jung and Karato, 2001). In the crust, seismic anisotropy can reflect pervasive, fluid-filled cracks or the crystallographic preferred orientation (CPO) of anisotropic minerals such as micas. However, most seismic interpretations are based on data compiled from various regions, and few studies (e.g. Zhong et al., 2014) have examined in situ rock properties to interpret seismic velocity models.

In a recent paper, Cossette et al. (2015) used textural data from rock samples collected at an exposed crustal-scale detachment zone (the West Cycladic Detachment System) in the West Cyclades of Greece to study the in situ seismic properties of various lithologies. Mineral CPOs were measured using the Electron Backscatter Diffraction (EBSD) techniques to derive seismic anisotropy that can then be used to constrain seismic velocity profiles in this region. The aim of this study is to constrain the structure and anisotropy of the crust in the Cyclades using a combination of seismic data and in situ rock properties. We use teleseismic receiver function data from an array of stations in the Aegean Sea to obtain a velocity model of the crust. Receiver functions are first processed using the harmonic decomposition method (Bianchi et al., 2010; Agostinetti et al., 2011; Audet, 2015) to visualize the lateral and vertical continuity of crustal structure and anisotropy across the array. We then calculate synthetic receiver functions based on seismic anisotropy data from Cossette et al. (2015) to reproduce first-order observations that emerge from the receiver functions and harmonic components, and discuss these results in the context of the tectonic evolution of the Aegean region.

3.3 Background and setting

The Cyclades form a group of islands situated in the center of the Aegean Sea (**Fig. 3-1**), in the back-arc region of the Hellenic subduction zone resulting from the convergence of the African Plate and the Eurasian Plate. The tectonic history of this region is characterised by

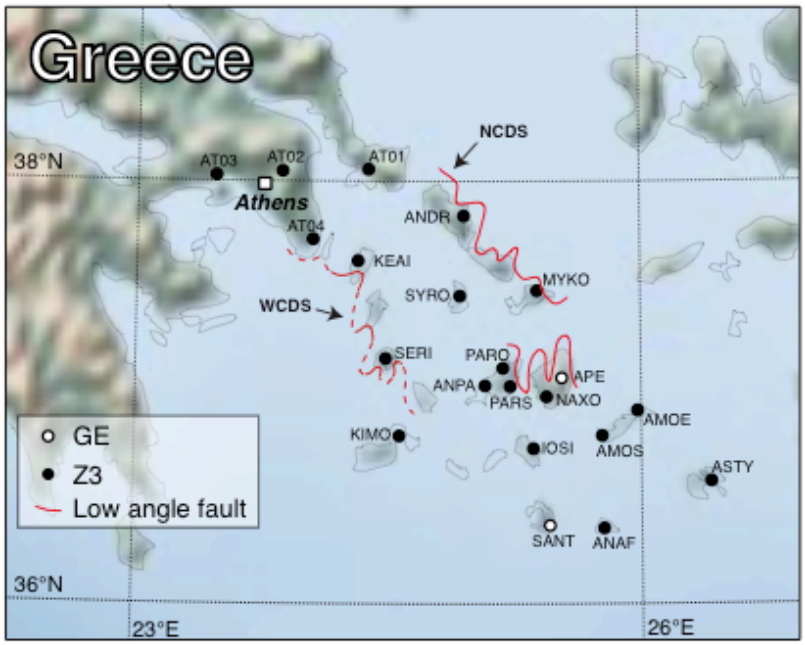

Figure 3-1. Map of the Aegean region showing seismic station locations of the GE and Z3 networks and the West and North Cycladic Detachment Systems (WCDS and NCDS)

the NNE sense of displacement of the African oceanic lithosphere subducting beneath the Aegean lithosphere. The now retreating African slab caused back-arc extension that started in the Oligocene and formed the Aegean basin (Gautier and Brun, 1994). The Cyclades were strongly affected by post-orogenic extension, where part of the exhumation during the Eocene revealed high-pressure (HP) rocks from deep portions of the orogeny, and another part that occurred during Oligocene-Miocene in the form of metamorphic core complexes (MCCs) (Jolivet and Brun 2008). Complex kinematics describe the relative motion of the Aegean micro-plate compared to Eurasia: in the middle Miocene, it underwent clockwise rotation in the western Aegean and counter-clockwise rotation in the eastern Aegean, whereas the central Aegean behaved as a coherent block (Kissel and Laj, 1988; Walcott and White, 1998). A uniform NNE-SSW orientation of stretching lineations is recorded across the Aegean MCCs when restored before the Miocene rotations (Morris and Anderson, 1996). The Cyclades expose the Attic–Cycladic Crystalline Complex, which classically comprises three geologic units (Bonneau, 1984, and references therein). The lowermost unit is the Paleozoic paragneiss and orthogneiss Cycladic basement intruded with Triassic granitoïds, which is overlain by the Cycladic blueschist unit, a polymetamorphic Carboniferous–

Permian to latest Cretaceous passive-margin sequence (e.g., Dürr et al., 1978; Blake et al., 1981). Some of the blueschists and eclogites that formed during the Hellenic orogen are now exposed on Syros and Sifnos islands. The Upper unit forms various klippens across the Aegean islands with relics of ophiolites, granitoids, Cretaceous metamorphic rocks and unmetamorphosed carbonates (e.g. Altherr et al., 1994; Katzir et al., 1996; Reinecke et al., 1982; Trotet et al., 2001; Skarpelis et al., 2008).

Large-scale deformation in the Aegean region created significant and coherent rock fabrics throughout the crust and mantle. Associated textures such as crystallographic preferred orientation give rise to seismic anisotropy that may be detected using seismological methods. Seismic anisotropy of the crust and mantle in the Aegean has been studied in the last decade using various data and techniques. Hatzfeld et al. (2001) studied the shear wave anisotropy of the upper mantle using the splitting of SKS phases and found that there is significant anisotropy in the north Aegean Sea that corresponds to current strain indicators obtained from GPS measurements. They suggested that the crust and mantle deformed similarly and that the fast polarization directions of the upper mantle did not relate to the surface expression of lithological fabric. Evangelidis et al. (2011) complemented this study with different computation methods and found good correlations between fast anisotropy directions and restored stretching lineations of MCCs. A receiver function study by Li et al. (2003) proposed the presence of 8% anisotropy in the crust to explain the polarity reversal observed on the transverse component at the Santorini station. Surface wave dispersion measurements (Endrun et al., 2008) point to spatial variation of radial shear-wave anisotropy in the Aegean, with the data strongly indicating 4.0-7.7% of anisotropy in the lower crust. Moreover, layered azimuthal anisotropy has been documented in the upper mantle and the crust (Endrun et al., 2011) by Rayleigh wave analysis. More specifically, they suggest that the lower crust in the Cyclades is characterised by 3.5% azimuthal anisotropy, due to an anisotropic fabric corresponding to the direction of Miocene extension. Apart from seismic studies, a textural investigation was conducted by Cossette et al. (2015) to describe seismic anisotropy in exhumed rocks along a detachment in the Cyclades. They found an average of 9.8% and 7.2% of P-wave and S-wave anisotropy, respectively, in upper crustal rocks, and increased values of 20.3% and 12.4% in the blueschist component of lower crustal rocks.

Their results were well approximated by anisotropy with a slow subvertical axis (50° to 85° for most samples), which is consistent with strong radial anisotropy and weaker azimuthal anisotropy, with the maximum P-wave velocities also corresponding to the direction of Miocene paleo-extension.

3.4 Methods

3.4.1 Receiver functions

Receiver functions are calculated for 21 stations in the Aegean, from continental Greece (Athens) to several islands North of Crete (**Fig. 3-1**). Two permanent broadband stations of the Geofon (GE) network provided data from 2007 and 2008 to 2014, and the 19 other temporary broadband stations of the EGELADOS (Z3) temporary network provided data from 2005 to 2007. We specifically selected these stations because we have in situ rock textural data representative of the Cycladic region only (Cossette al., 2015).

A first set of receiver functions was calculated from teleseismic P waves, using earthquake events with a magnitude > 5.6 occurring at an epicentral distance between 30 and 90° of each station. For two stations of the GE network (SANT and APE), the dataset was complemented with receiver functions calculated from PP waves, using events with a magnitude > 6 and epicentral distances between 60 and 130°. Waveform data were extracted 120 s before and after the arrival time of the direct P-wave. Seismograms with signal-to-noise ratio (SNR) lower than 5 dB on the vertical component in the 0.05-1 Hz frequency band were discarded. The horizontal component data were first rotated into radial and transverse components. The vertical and horizontal components were then decomposed into upgoing P (compressional), SV (shear radial) and SH (shear transverse) wave modes following Kennett (1991) and Bostock (1998), and using Vp = 6 km/s and Vs = 3.5 km/s, to partially remove the effect of the free surface and isolate the direct P-wave onto a single component of motion. Individual single-event seismograms were then processed to produce receiver functions by deconvolving the P component of motion from both SV and SH components. Deconvolution is performed in the frequency domain using a Wiener filter that takes into account pre-event noise on both vertical and horizontal components to correct for tilting effects (Audet, 2010).

Following deconvolution, we further discarded anomalous large amplitude and oscillatory data using a root-mean-square criterion. The final receiver functions were stacked into back-azimuth and slowness bins of 10° and 0.002 s/km, respectively.

Receiver functions represent P-to-S converted signals generated from discontinuities in seismic velocity. If the crust were uniform and isotropic, with a flat Moho, the receiver functions would show no variation in radial amplitude with back-azimuth, and no energy would be converted on the transverse (SH) component. Wherever the receiver functions do display radial amplitude variations with back-azimuth and signal on the SH component, they imply structural heterogeneity (e.g. dipping discontinuity), elastic anisotropy, or both (Cassidy, 1992; Levin and Park, 1997; Savage, 1998; Frederiksen and Bostock, 2000; Audet, 2015). The receiver functions sample anisotropy or structural heterogeneity differently based on the azimuth and incidence angle of the ray path. For simple models of heterogeneity (dipping interface) and dipping hexagonal anisotropy with fast or slow axis of symmetry, we expect to see a 360° periodicity in amplitude with back-azimuth, and a 90° shift between SV and SH amplitudes (Bianchi et al., 2010; Audet, 2015).

Figures 3-2a and **c** show the receiver functions for stations APE and SANT, on Naxos and Santorini islands, respectively. Both stations have a back-azimuth coverage that allows seeing radial amplitude variations with back-azimuth. In particular, we observe differences in the arrival time of an early positive arrival (≤1 second) at station APE; between 225° and 325° of back-azimuth, this signal arrives at ~0.5 second, whereas between 325° and 160° it arrives at ~1 second. The transverse component displays polarity reversals at ~0.5 second around 140° and 320° back-azimuth. The radial component at station SANT also shows variations in arrival times, for example between 50° and 180° of back-azimuth, where we observe a positive arrival delayed from ~3.5 to ~4.5 seconds. There is significant energy on the transverse component as well, with several polarity reversals visible at 120° back-azimuth. These observations strongly suggest the presence of structural heterogeneity and/or elastic anisotropy in the crust.

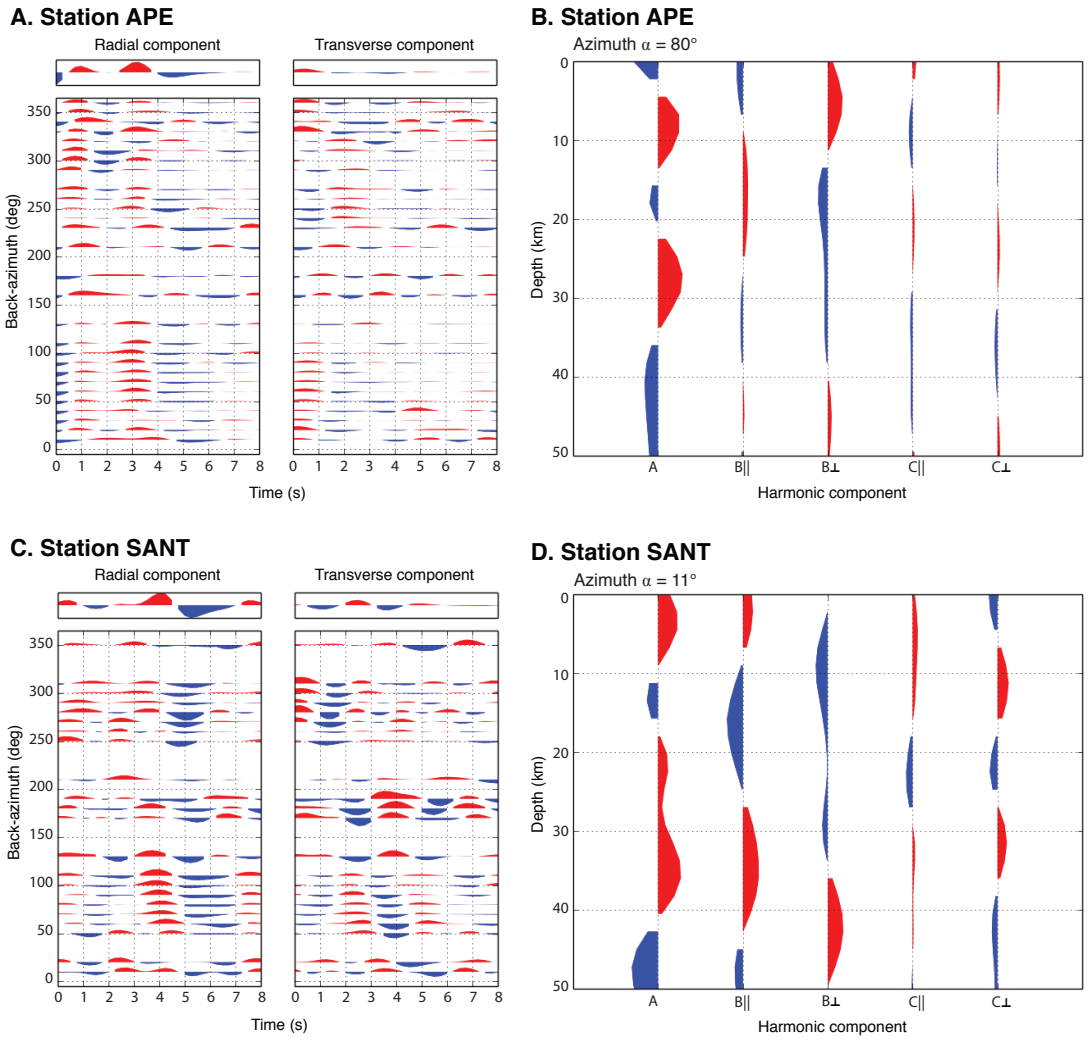

Figure 3-2. Receiver functions and harmonic decompositon for station APE on Naxos (A and B) and station SANT on Santorini (C and D). The azimuth α is the orientation obtained when the variance is minimised on BII.

3.4.2 P-wave ray angles

Stereonets showing the distribution of P-ray angles at Moho depth (~30 km) were determined in order to see if the receiver functions could resolve the anisotropy in the crust. Using the ray parameter and the back-azimuth of the P-waves, the corresponding trend and plunge of the rays were calculated and plotted for each station (**Fig. 3-3**). The P-ray points are concentrated in the center of the stereonet, with plunges around 60° (incidence angles of ~30°). Cossette et al. (2015) previously determined the P-wave velocity distribution from textural data in the West Cyclades – they reported maximum velocities occurring sub

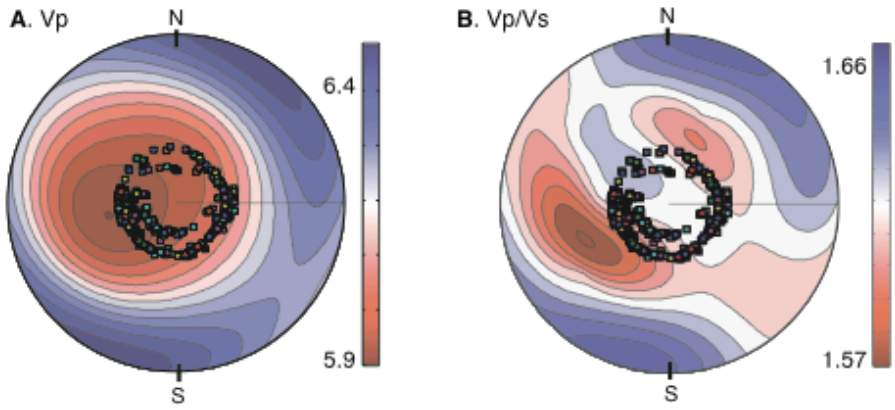

Figure 3-3. P-wave ray angle distribution at station APE superimposed on A: P-wave velocity (in km/s) and B: Vp/Vs ratio of metapelites in the Cyclades. The maximum and minimum velocities resolved by the P-rays are ~6.1 and ~5.9 km/s, respectively, giving a P-wave anisotropy of ~3.3%. Seismic figures are from Cossette et al. (2015) and represent data for one sample of the West Cycladic Detachment System

horizontally. Therefore, the P-ray points would necessarily resolve a seismic anisotropy lower than the total anisotropy for a given sample, since they only sample low P-wave velocities.

3.4.3 Migration

Post processing of receiver functions was performed in order to extract the information on structure and anisotropy of the crust. The receiver functions were first migrated from time to depth using a one-dimensional velocity model (**Table 3-1**) based on the calculated seismic velocities obtained from Cycladic rocks (Cossette et al., 2015). Since the Cyclades are free of sediments (Makris et al., 2013), P-wave velocities at the surface correspond to those of

Table 3-1. Velocity model for the migration to depth (modified from Bruestle, 2012 and Makris et al., 2013)

Depth (km)	Vp (km/s)	Vs (km/s)
0	6	3.55
2	6.5	3.82
26	6.6	3.86
30	7.5	4.31
37	7.8	4.48
47	7.86	4.49
60	7.92	4.52
85	8.13	4.64
125	8.42	4.81
175	8.43	4.82
225	8.43	4.82

metamorphic rocks characterised by high values (~6 km/s), and the Moho is located at approximately 30 km depth (e.g. Makris et al., 2013; Bruestle et al., 2012). The P-to-S velocity ratio (Vp/Vs) varies from values averaging 1.69 (Cossette et al., 2015) in the upper crustal section characterised by schists, marbles and quartzites and increases to higher values in the lower crust and mantle (1.73-1.75). We employ the equation of Dueker and Sheehan (1997) to migrate receiver functions over a depth range of 0 to 100 km.

3.4.4 Harmonic decomposition

We jointly analyse the SV and SH receiver functions by decomposing them into back-azimuth harmonics following the method described in Bianchi et al. (2010) and modified by Audet (2015). In this process, the sets of SV and SH traces are expressed as sums of $\cos(k\varphi)$ and $\sin(k\varphi)$, where k is the harmonic degree (here k is 0, 1, or 2) and φ is the back-azimuth. The resulting five harmonic terms (1 for k=0, 2 each for k=1 and k=2) thus represent the back-azimuth variations in the amplitude of SV and SH resolved onto each harmonic degree. The first term A represents the amplitude of the SV signal that does not vary with back-azimuth (k=0); it therefore represents signal originating from background velocity contrasts onto which anisotropy or heterogeneity is superimposed. The two terms B correspond to one periodicity with back-azimuth (k=1) for two normal orientations (B|| and B⊥), and indicate the presence of either a dipping interface or an anisotropic layer with a plunging symmetry axis (Bianchi et al., 2010; Agostinetti et al., 2011; Audet, 2015). The two terms C correspond to two cycles with back-azimuth (k=2) and indicate anisotropy with a horizontal symmetry axis (Levin and Park, 1997; Shiomi and Park, 2008).

Here we minimised the energy on the second component (i.e. where the variance is minimal on B||) in order to estimate the azimuth α for which $\varphi - \alpha = 90°$. This azimuth corresponds either to the strike of a dipping interface or to the orientation of the fast axis of symmetry of an anisotropic medium. The depth range over which the orientation α was determined is from 0 to 30 km depth, roughly corresponding to the Moho. This procedure limits our ability to characterize intra-crustal variations in the orientation of anisotropy, and the recovered azimuth therefore represents the orientation of the dominant source of anisotropy in the crust.

Figures 3-2b and **d** show the harmonic decomposition for stations APE and SANT. The terms A (k=0) correspond to the migrated SV components stacked over all back-azimuths (**Fig. 3-2a** and **c**), and show the velocity contrasts that do not vary with back-azimuth. On the other components, stronger amplitudes correspond to a preferred orientation (α in this case). For station APE, there is very little energy on the C terms, which allows us to discard the presence of anisotropy with horizontal symmetry axis. The energy was minimised on B|| (with an obtained orientation α of 80°), thus the signal is dominantly projected onto B⊥. On Santorini (SANT), the C terms contain less energy compared with the A and B terms, again indicating a dipping interface or anisotropy with a plunging axis of wave propagation. Although the variance was minimised on B|| (with an estimated α of 11°), there are still significant amplitudes of SV and SH variation with back-azimuth, and a single trend of symmetry axis for the entire depth range could not be found. Although the harmonic terms for SANT are ambiguous compared with those for station APE, these results suggest the presence of a dipping layer and/or anisotropy with a plunging axis instead of anisotropy with a horizontal axis.

3.4.5 Synthetic models

We generated synthetic receiver functions by modelling plane wave propagation through a stack of homogeneous, anisotropic layers using the reflectivity technique of Kennett (1983) and Thomson (1996). Each layer is defined by its thickness, density, P and S wave velocities. Anisotropy is modelled as hexagonal symmetry with either a fast or slow axis of symmetry, and is parameterized by the percent anisotropy and the trend and plunge of the symmetry axis. Parameters used in 1-D velocity models are based on seismic properties constrained by in-situ rock properties described by Cossette et al. (2015) and structural information (e.g., depth to discontinuities) constrained by the receiver function data. Synthetic receiver functions are calculated at the same back-azimuth and slowness range as the observed data. Each set of receiver functions is further processed using the harmonic decomposition to compare with the observed harmonic terms. The objective of the modelling is to reproduce the calculated receiver functions using anisotropy information from textural data. We calculate the root-mean-square error (**Table 3-2**) between the calculated and synthetic

receiver functions over the first 5 seconds in order to quantitatively evaluate the fit to receiver function data.

3.5 Results

3.5.1 Receiver functions

Figure 3-4 shows the radial component receiver functions stacked over all back-azimuths in the time domain and migrated to depth in order to visualize the main features of the data. The positive arrival at ~3 seconds corresponds to the downward increase in velocity at the crust-mantle interface, which varies between 22.5 to 33 km depth across the array. Although not shown here, a second positive pulse with similar amplitude is found between 10 and 11 seconds, followed by a negative arrival at 12-13 seconds, which correspond with the free-surface reverberations. At ~1 second, a set of positive arrivals can be detected, corresponding to a downward increase in velocity at a depth of approximately 3 to 11.5 km. There seems to be an additional negative arrival at ~ 4.5 seconds, corresponding to a downward decrease in velocity at depths of 40-50 km. The double positive-negative pulses between ~3 to 4.5 seconds may indicate a ~10 km high-velocity mantle lid immediately below the Moho, sandwiched between the low velocity crust and underlain by normal velocity mantle. In this paper we focus on results for the crust and ignore deeper structure.

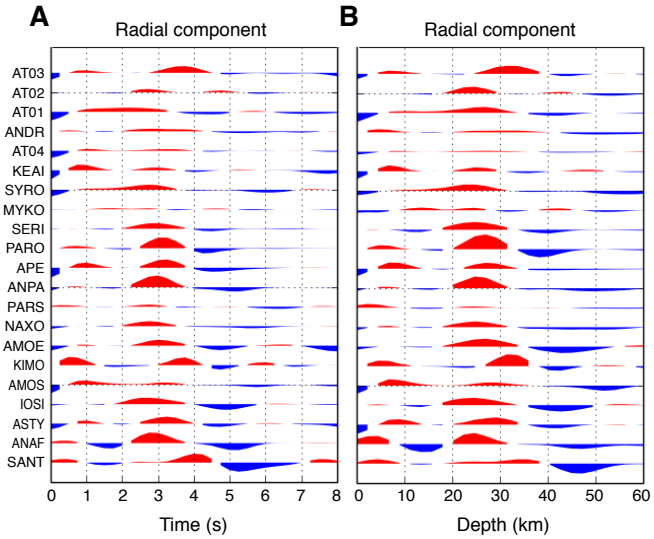

Figure 3-4. Receiver functions for the 21 selected seismic stations of the Cyclades in function of A: time and B: depth

3.5.2 Harmonics

Figure 3-5 shows the corresponding variations in the five harmonic components, sorted by station location from north to south. The A term (k=0) shows two horizontal interfaces with positive velocity contrasts (**Fig. 3-5a**) identical to the stacks of radial component of the migrated receiver functions (**Fig. 3-4b**). The shallower discontinuity, clearer in the southern part of the profile, appears almost continuously and is found at depths of 3 to 11.5 km. The second discontinuity is found at depths varying from 22.5 to 33 km. This discontinuity is better defined under the southern stations (i.e. south-central Aegean), from KEAI to SANT, where it is relatively horizontal (average depth of 25.5 km). Beneath the northern stations, the discontinuity is not as clear and seems to occur a little deeper with a reduced velocity contrast.

Figure 3-5b and **c** show the B|| and B⊥ components, respectively, that reflect periodicities of 360° in back-azimuth. Since we minimise the energy on the B|| component in order to find α, we find insignificant energy on this component, indicating that the anisotropy is coherent within the crustal column. The B⊥ harmonics show features that suggest the presence of either dipping interfaces or anisotropic layers that are subhorizontal in the central and southern parts of the profile and appear to be deepening toward the north. Positive amplitudes are found at a depth of ~50 km toward the north and gently rise up and flatten out at depths of ~32 km. Just above, we find negative amplitudes with the same shape arriving at depths of ~38 km in the north, rising up and flattening to depths of ~18 km in the central part. These amplitudes produce a polarity reversal, best seen in the south-central Aegean, occurring at the same depth as the second discontinuity on the A component (i.e. at 25.5 km depth). Positive amplitudes are also observed at shallow depths, around 5-12 km. Interestingly, the azimuths α for which the energy is minimised on the B|| component do not show any consistent orientation – rather, they sample orientations between 0 and 360°.

The harmonics with k=2 (**Figure 3-5d, e**) do not contain significant energy and are comparatively noisy. It is interesting to note, however, that the C⊥ component yields similar patterns as in the B⊥ component, with positive and negative arrivals that are deeper in the north and shallower in the central and southern parts.

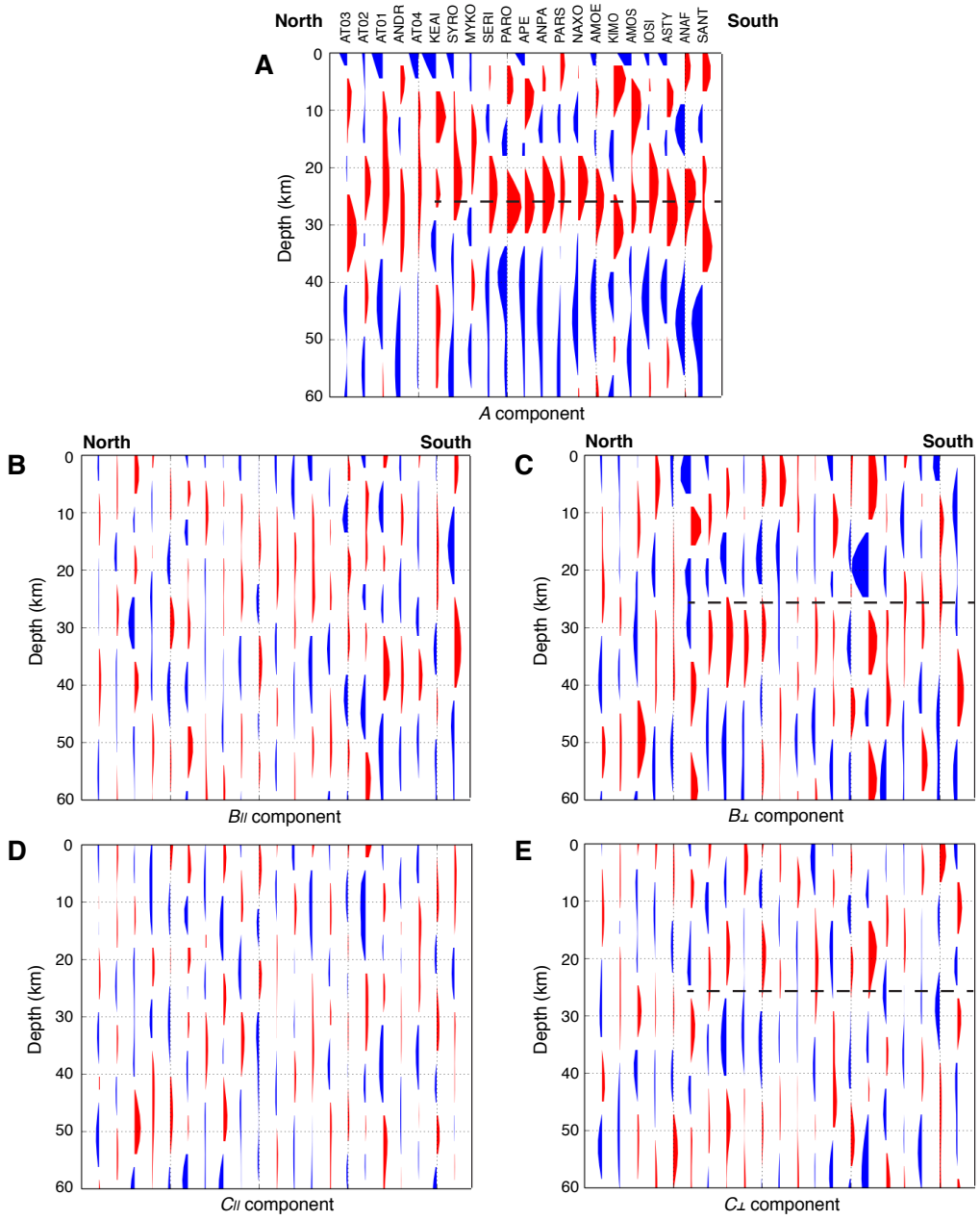

Figure 3-5. Harmonic decomposition for the 21 selected seismic stations in the Cyclades. A-E: harmonic components A, B_{ll}, $B_{\perp}$, C_{ll} and $C_{\perp}$. Dashed line on the term A harmonics corresponds to the Moho, and we note that it lies in the middle of a polarity reversal on the term $B_{\perp}$.

3.5.3 Receiver function modelling

The harmonic terms are useful in the visualization of lateral and depth variations in directional properties but provide limited insight into the source of the anisotropy. We perform synthetic modelling of receiver functions at station APE because it has a good back-

azimuth coverage and high signal-to-noise ratio, allowing seeing polarity reversals that suggest the presence of anisotropy. This station yields two positive arrivals on the radial component stacks, at depths of ~7 km and ~27 km (**Fig. 3-2a, b**). In order to reproduce these two discontinuities, we tested several models taking into consideration the geology of the Aegean, in order to create two velocity jumps at 7 and 27 km. The lithology of the region comprises blueschist and eclogite rocks from the Cycladic Blueschist unit, which are characterised by faster seismic velocities than the metapelites and marbles and thus appropriate for a velocity increase at 7 km. The extension that led to the formation of the metamorphic domes in the Aegean allowed only a small part of these HP rocks to be exhumed. It is likely that we find the same lithotype at shallow depth, overlying the Cycladic basement composed of schists and orthogneiss (Andriessen et al., 1987). At 27 km depth, we expect the Aegean lithospheric mantle and therefore assign mantle values below this interface. Below we present 6 models (**Table 3-2, Fig. 3-6**) and describe briefly how the synthetic receiver functions were affected by the variation of specific parameters.

Table 3-2. Synthetic model parameters for station APE

Model	Layer thickness (km)	Density (kg/m^3)	Vp (km/s)	Vs (km/s)	% Anisotropy	Symmetry axis	Trend/plunge (deg)	Azimuth α (deg)	Least square fitting SV	Least square fitting SH
1	7	2820	6.21	3.70	10	slow	320/60	88	9.496E-08	5.530E-08
	20	3250	7.50	4.40	-	-	-			
	60	3240	7.80	4.45	-	-	-			
2	7	2820	6.21	3.70	10	slow	140/60	82	9.543E-08	6.440E-08
	20	3250	7.50	4.40	-	-	-			
	60	3240	7.80	4.45	-	-	-			
3	7	2820	6.21	3.70	10	slow	330/60	81	9.370E-08	5.582E-08
	20	3250	7.50	4.40	-	-	-			
	60	3240	7.80	4.45	-	-	-			
4	7	2820	6.21	3.70	5	slow	330/60	81	9.309E-08	5.358E-08
	20	3250	7.50	4.40	0	-	-			
	60	3240	7.80	4.45	0	-	-			
5	7	2820	6.21	3.70	5	slow	330/60	85	9.273E-08	5.133E-08
	20	3250	7.50	4.40	5	fast	320/60			
	60	3240	7.80	4.45	0	-	-			
6	1	3000	7.00	3.00	5	slow	330/60	85	7.120E-08	5.489E-08
	6	2820	6.21	3.70	5	slow	330/60			
	1	3050	7.00	4.00	10	slow	330/60			
	19	3250	7.50	4.40	5	fast	320/60			
	60	3240	7.80	4.45	0	-	-			

Model 1 (**Fig. 3-6a**) is the most simple and is based on the observation of a polarity reversal at 140° and 320° on the transverse component of station APE. In the first layer we use a slow axis of symmetry, as found in most minerals in the upper crust with a hexagonal symmetry approximation (e.g. Lloyd et al., 2009; Erdman et al., 2013), trending 320° with a plunge of

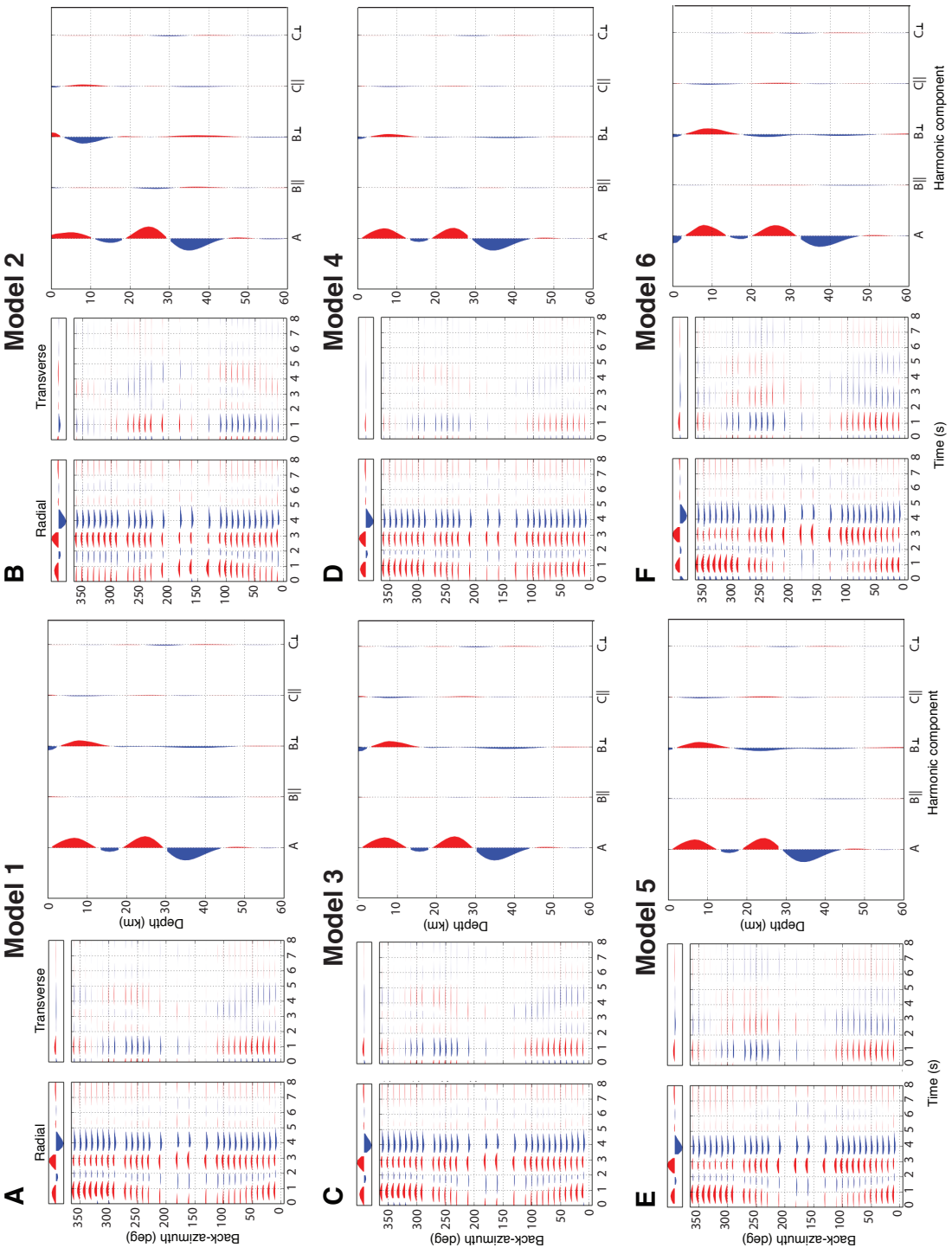

Figure 3-6. A-F: Synthetic receiver functions (left) and harmonic decompositon (right) for models 1 to 6.

60° and no more than 10% anisotropy (Cossette et al., 2015). The lithology corresponds to metapelites with seismic velocities calculated from EBSD data (**Table 3-2**). The second layer has an average of blueschist and eclogite seismic velocities (Bezacier et al., 2010; Cossette et al., 2015), and this layer is isotropic for simplicity. Synthetic receiver functions for this model show positive arrivals at ~1 second and ~3 seconds, similar to calculated receiver

functions at station APE (**Fig. 3-2a**). The amplitude at 1 second is smaller than the one at 3 seconds, consistent with the observations. On the transverse component of the synthetic receiver functions, the polarity reversals are reproduced at 1 second and at back-azimuths of 140° and 320°, compared with ~0.5 second for the observed data. The general pattern, especially the negative amplitudes from 2 to 5 seconds, between 0° and 140° back-azimuth, also matches the calculated receiver functions. The harmonic decomposition shows that the high velocity layers are located at 7 km and 25 km. There is no energy on B|| (α = 88°) and B⊥ has a positive pulse at ~8 km depth, as in the observed data.

Model 2 (**Fig. 3-6b**) has the same parameters as Model 1, except for a trend of symmetry axis that is now 140°. The resulting receiver functions show the same radial stack as in Model 1, although the variations in SV amplitude with back-azimuth are different. There is a good match between the synthetic and calculated receiver functions for the positive amplitudes at 0.5-1 second, between 75° and 300° back-azimuth. However, between 300° and 75° back-azimuth, the synthetic receiver functions yield earlier arrival times. The transverse components show a pattern that does not correspond to the observed one. Even though the polarity reversals occur at the right back-azimuths, they are of opposite sign. The harmonic decomposition allows us to find an azimuth α of 82° when energy is minimised on B||, very similar to the α of 80° at station APE. Although α is very similar, the least square values are higher compared to Model 1.

In Model 3 (**Fig. 3-6c**) we explored the effect of changing the azimuth of the symmetry axis. We found that increasing the azimuth to 350° yields a better fit to the radial component, but a worse fit to the transverse component. Furthermore, a quite different orientation α of 67° is obtained. When decreasing the azimuth to 310°, the fit to the SV component is much worse, whereas the SH component fit decreases only slightly. We found that an azimuth of 330° was the best estimate, with an orientation α of 81°, very similar to the α at station APE.

Varying the anisotropy in the upper crust, in Model 4 (**Fig. 3-6d**), allowed us to find that the fit to the SV and SH components rapidly decreases with higher values of anisotropy. The

best fit was obtained with an anisotropy of 5%; values lower than 5% also lead to a poorer fit.

Model 5 considers anisotropy in the second layer. Since the seismic anisotropy of eclogite is well approximated with hexagonal symmetry with a slow axis and is very weak (1-4%, Bezacier et al., 2010; Worthington et al., 2013), we first modeled slow anisotropy of 1-3% in the second layer, which gave a poor match between calculated and synthetic receiver functions. On the other hand, we obtained better results when modelling anisotropy <5% with a fast axis of symmetry (**Fig. 3-6e**). The transverse component shows more obvious negative amplitudes between 0° and 100° back-azimuth, at 1.5-2 seconds, similar to what is found at station APE. Moreover, the fit was better with an azimuth of 320° instead of 330° for the fast axis of symmetry. The harmonic decomposition for this model yields an orientation α of 85°, and the B⊥ term now displays a double polarity as found at station APE.

We made other observations that are not compiled in the table, but are summarised here. Adding a 1 km thick layer of higher velocity (i.e. 6.5 km/s) at the surface with the same anisotropy (5%) as in the metapelites increases the fit of the SV component without much affecting the SH component. It allows creating the negative amplitudes observed at 0-0.5 second on the APE receiver functions. Using more gentle plunges for the symmetry axis creates a worse match. Steeper plunges attenuate the effect of anisotropy and obliterate the patterns on the transverse component. A thin layer of high anisotropy (10%, which could correspond to very anisotropic blueschist) just above the 20 km thick layer notably increases the fit of the SV component, and decreases only by a little the fit of the SH component. Model 6 (**Fig. 3-6f**) is an attempt for a more complex model accounting for these observations and comprising many parameters. It includes a thin layer of high velocity at the surface, 6 km of anisotropic metapelites, 1 km of high anisotropy (with densities and velocities corresponding to blueschist) and 19 km of dense material with a fast axis of symmetry for the anisotropy. This creates the best fit for the radial component, whereas the transverse has an acceptable fit as well relative to the other models.

3.6 Discussion

The radial component stacks of the receiver functions and the A harmonic terms all point to a discontinuity at 22.5-33 km depth, characterised by a sharp downward velocity increase that likely corresponds to the Moho, with the south-central Aegean showing a relatively flat Moho with an average depth of 25.5 km. Similar Moho depths of 25-29 km have been documented in the northern and central Aegean (Bohnhoff et al., 2001; Tiberi et al., 2002; Li et al., 2003; Tirel et al., 2004; Sodoudi et al., 2006, 2013; Makris et al., 2013). Low crustal thicknesses are likely caused by back-arc extension associated with elevated sub-crustal temperatures. These results are consistent with the thermal isostasy model of Hyndman and Currie (2011) that relates low crustal thickness in back-arc regions to uniformly high elevation that is supported by a hot, buoyant mantle. This model predicts a crustal thickness of ~27 km in back-arcs where the elevation is at sea level (compared to ~38 km in a stable craton), indicating that the mantle beneath the Aegean Sea may be on average 250°C hotter compared to mantle temperatures beneath cratons, from the surface down to ~200 km depth. Moreover, we find the thinnest crust (22.5 km) for the islands of Ios and Naxos, which are high temperature domes. Andros, which only experienced moderate heating during the Eocene (Jolivet and Brun, 2008), has a higher crustal thickness of 29 km and stations AT01, AT03 and AT04, on the continent, also have thicker crusts varying between 27 and 32 km.

The harmonics with an order k=1 (in particular, B⊥) give insights into the depth and lateral variations in the anisotropic structure, and show a deepening of a double-polarity pulse from south to north. These signals seem to mirror the ones of the A harmonics, where the Moho appears to be deeper in the north as well, and where the Moho overlaps the double polarity observed on the B⊥ component. The origin of the deepening double-polarity layer to ~50 km depth on the B⊥ component is ambiguous and may represent a north-dipping low-velocity zone or a dipping layer of anisotropic material. However the Hellenic slab is >75 km deep in the southernmost portion of the array, with greater depths toward the north (Li et al., 2003; Sodoudi et al., 2006) thus the double-polarity pulses cannot be directly linked with the subducting crust of the African lithosphere. Moreover, the Aegean Moho is documented to be relatively flat in the Aegean back-arc basin (e.g. Tirel et al., 2004) and the estimated

azimuths α are not consistently oriented with the strike of a single dipping interface. Li et al. (2003) reported that at station SANT, an unlikely dip of 40° of the crust-mantle interface would be needed to resolve the variation in arrival times at the Moho, thus favouring the hypothesis of elastic anisotropy. This suggests the presence of an anisotropic layer rather than a dipping interface, although we cannot rule out the occurrence of dipping layers with our data. Mineral anisotropy is strongly expected due to the presence of pervasive stretching lineations related to ductile flow in the weakened lower crust during the exhumation of metamorphic core complexes in the Cyclades (Jolivet et al., 2013). At the observed depth of the polarity reversal, however, anisotropy would most likely be related to flow in the mantle lithosphere, oriented parallel to the current strain field of extension (Endrun et al., 2011).

The azimuths α obtained from the minimization of variance on the B|| component represent either the strike of a dipping interface or the orientation of the fast axis of symmetry in anisotropic materials with hexagonal symmetry. Our data yield azimuths ranging between 0 and 360°, suggesting that the trend of the anisotropy is not coherent across the array of stations. However this apparent scatter may be expected for a subvertical axis with very steep plunges, where the trend of the anisotropy axis is more difficult to resolve and indicating that the symmetry axis is dominantly vertical. This is consistent with the study by Cossette et al. (2015), where a slow subvertical axis of wave propagation was the best approximation for the observed seismic anisotropy. The trend of the slow symmetry axis is obtained by adding 90° to the azimuth α. The harmonic decomposition performed here also corroborates the result of a subvertical axis, since a horizontal axis of symmetry would be mostly observed on the C component. Finally, the energy still present on the B|| component at some stations when we minimise the variance suggests that there are likely different anisotropic layers with slightly different trends of symmetry axis at various levels within the crust.

It is worth mentioning that the seismic velocity models are not unique as several models could fit the calculated data almost equally well. These ones can become rapidly complex when defining several layers with many parameters, thus we preferred to focus on the simplest ones. Our models require a thick layer of ~20 km of almost constant and high velocity in order to create two velocity jumps similar to the ones observed at station APE.

There is evidence that the Cycladic basement experienced HP metamorphism, later than the HP metamorphic episode of the Cycladic blueschist (Ring et al., 2001 and references therein), that could explain the presence of dense and high-velocity material beneath the upper crust. Besides, due to a large amount of extension (700 km, Jolivet and Brun, 2008), the Cyclades experienced Miocene magmatism (e.g. on Serifos, Naxos, Tinos, Mykonos islands) and we can speculate that partial melting probably created a restite in the lower crust, which would have higher seismic velocities since it would be depleted in low-temperature (i.e. low velocity) minerals like muscovite, K-feldspar and quartz. However not all stations in the Cyclades require this thick layer of high-velocity material, as shown by the downward velocity decrease around 1.5-2 seconds (~15 km depth) at station ANAF, for example.

In the central Aegean mantle lithosphere, seismic anisotropy has been found to be small (Endrun et al., 2011), consistent with this region having undergone little deformation in the last 20 Myr. Our data point to the same result, where the best (and simplest) models comprise only 5% of anisotropy in the upper crust. This is also consistent with steep incident P-rays sampling only low values of anisotropy (**Fig. 3-6a**). It appears that <5% anisotropy with a fast axis of symmetry is needed in the 20 km thick lower crustal layer in order to reproduce the double polarity on the B⊥. This is rather unexpected, since most minerals in the upper to lower crust are well approximated by hexagonal anisotropy with slow axis of symmetry. It has nonetheless been found in other receiver function studies that lower crust anisotropy was best reproduced with fast axis symmetry (e.g. Sherrington et al., 2004; Tian et al., 2008).

The fact that we find slow and fast symmetry axes of anisotropy makes the meaning of the orientation α ambiguous. Although the synthetic models find an azimuth α very similar to the 80° obtained at station APE, it cannot represent the orientation of both slow and fast axes at the same time, since they are shifted by 90°. A test was conducted for station APE using a depth range of 7 km (corresponding to the metapelite layer thickness) for the calculation of α in the harmonic decomposition. The orientation obtained is 102°, which means that a slow axis of symmetry would be oriented at 192° for the upper crust characterised by metapelites.

This is consistent with the NE-SW orientation of Miocene paleo-extension, and also with the maximum velocity and anisotropy orientations calculated from EBSD data for the same rocks (Cossette et al., 2015). It likely explains why α varies so much across the array of stations, since it depends on the proportion of anisotropy between lower and upper layers. It further reinforces the notion of complex anisotropy layering in the crust as demonstrated by Endrun et al. (2011). Our study shows that layering occurs at the kilometer scale.

Numerous assumptions need to be made in numerical modelling of receiver function data. In these synthetic models, the anisotropy is assumed to follow a pure ellipsoid, with similar percent P and S anisotropy (Porter et al., 2011). However, as calculated from EBSD measurements (e.g. Lloyd et al., 2009; Bascou et al., 2011; Bezacier et al., 2010; Dempsey et al., 2011; Cossette et al., 2015), very few lithotypes show pure ellipticity for P- and S-waves. Blueschist, for example, has an average P-wave and S-wave anisotropy of 20.3% and 14.5%, respectively. Moreover, the anisotropy in the crust is far from being homogeneously distributed on a vertical profile, with layers possessing differences in anisotropy as high as 20% on the <km scale, depending on the orientation of the upcoming P-wave (Cossette et al., 2015). There are also probably large sources of error due to the strong dependence of the receiver functions on the Vp/Vs ratio, which varies strongly with the orientation of incoming P-waves (Cossette et al., 2015). From the resolved ray points of the P-waves and Vp/Vs plots of Cycladic rocks, we observe that the seismic rays are likely to sample the lowest values of Vp/Vs (**Fig. 3-6b**). Reducing the Vp/Vs ratio to 1.6-1.65 in the first 20 km of the velocity model would affect the migration process, and would lower down the depth of the Moho by about 2 km. In the case of station APE, using this Vp/Vs ratio yields a more accurate Moho depth of 27 km. This demonstrates the importance of using in situ rock seismic properties oriented in the field. In fact, it is shown here that upcoming P-waves will resolve very heterogeneous values of anisotropy and Vp/Vs ratio. The good match between the calculated and synthetic receiver functions thus provides constraints on the source of seismic anisotropy in relation with in situ rock textural data, and the modeled seismic profiles confirm that we can use teleseismic receiver functions to map lateral variations in the crust.

3.7 Conclusion

We employed teleseismic receiver functions of the Cyclades to constrain the layered structure and anisotropy in the crust. A Moho depth of 22.5 to 33 km with an average of 25.5 km in the south-central Aegean is found, as well as a sharp downward velocity increase at 3-11 km depth. The crust is thinner beneath the high-temperature domes of Naxos and Ios, and is thicker close to the continent. Back-azimuth harmonic decomposition points to intracrustal anisotropy best approximated with a plunging axis of symmetry. We use two discontinuities observed at depths of 7 and 27 km at station APE to create synthetic models that include seismic properties of rocks calculated from EBSD data. Our models indicate that the upper crust is characterised by ~5% anisotropy with a slow axis of symmetry, with velocities corresponding to the ones of metapelites. Below the upper crust, a ~20 km thick layer of dense material with high seismic velocities is needed to reproduce the observed data. Anisotropic layering is indicated both by the synthetic modelling and the harmonic decomposition, with this second layer possibly possessing 5% of anisotropy as well. Our study stresses the importance of considering in situ rock textural data for seismic velocity profile interpretation, which can help map lateral variations in crustal structure.

4. CONCLUSION

Our study aimed to resolve the contribution of mineral seismic anisotropy to seismic velocity profiles. In our first article, we determined the seismic properties of rock samples along a detachment in the Cycladic region of Greece. Muscovite and glaucophane show strong crystallographic preferred orientations that have a control on the average seismic anisotropy of the rocks. Our results suggest that radial seismic anisotropy is stronger than azimuthal anisotropy, and a slow axis of symmetry produces a good estimate for the resulting anisotropy. An aspect of our results that happened to be significant in the light of the second paper is the heterogeneity of the seismic properties in function of orientation. The Vp/Vs ratio, for instance, is commonly assumed to be homogeneous in the crust for simplicity, but our results contradict this assumption. Moreover, although high anisotropies were calculated from the textural data, the P-rays in this study could only sample low magnitudes of anisotropy due to their incidence angle.

Some aspects of our textural investigation could possibly be improved: we only sampled the West Cycladic Detachment System, which may not be representative of the whole Aegean region. Notably, we did not incorporate igneous rocks from Miocene intrusions in some of the metamorphic core complexes. These rocks are likely the ones that could give different average anisotropies, since their mineralogy is much different, with more quartz and feldspar from a granodioritic composition. We hypothesise that the resulting anisotropy would be lower, since the randomly oriented crystals in an igneous rock yield more isotropic properties.

The receiver functions from several stations in the Cyclades indicate that the Moho lies at an average depth of ~25 km. The crust is thinner above hot metamorphic domes and is thicker toward the continent. A layer of high velocity material is found at depths varying between 3 and 11 km, and possibly corresponds to high-pressure metamorphic rocks or material depleted in low-temperature minerals. The synthetic receiver functions point to an upper crust possessing ~5% anisotropy with a slow axis of symmetry. Anisotropy in the crust is

complex, as several anisotropic layers are needed to best reproduce the calculated receiver functions.

Gaining more precision about the extent and orientation of anisotropy in the crust is the aspect that needs the most improvement. In fact, our modelling investigation yields discrepancies between the trend of the symmetry axis used to reproduce the calculated receiver functions and the one obtained from the harmonic decomposition. Although this discrepancy is a result by itself likely indicating layering of anisotropy in the crust, there is place for progress. Using higher frequencies in the modelling part could be an avenue, as it may yield more precision in the calculation of the azimuth α over smaller kilometer ranges in the harmonic decomposition.

Finally, CPO seismic anisotropy proves to be an important factor to consider when interpreting seismic velocity profiles. Seismic properties (from textural analyses) need to be oriented in the field to yield valuable information that can then be used to constrain velocity models. These velocity models produce better results when employing calculated velocities from rock samples, and more importantly, Vp/Vs ratios and anisotropy data according to the P-rays incidence angle.

REFERENCES

Agostinetti, N. P., Bianchi, I., Amato A., and Chiarabba, C., 2011. Fluid migration in continental subduction: The Northern Apennines case study, Earth Planet. Sci. Lett. 302, 267–278.

Alexandrov K.S., and Ryzhova T.V., 1961. Elastic properties of rock-forming minerals. II. Layered silicates. Bulletin of the Academy of Sciences of the USSR, Geophysics Series 9, 1165–1168.

Aleksandrov, K.S., Alchikov, U.V., Belikov, B.P., Zaslavskii, B.I., Krupnyi, A.I., 1974. Velocities of elastic waves in minerals at atmospheric pressure and increasing precision of elastic constants by mean of EVM (in Russian). Bulletin of the Academy of Sciences of the USSR, Geophysics Series 10, 15–24.

Altherr, R., Schliestedt, M., Okrusch, M., Seidel, E., Kreuzer, H., Harre, W., Lenz, H., Wendt, I., Wagner, G.A., 1979. Geochronology of high-pressure rocks on Sifnos (Cyclades, Greece), Contrib. Mineral. Petrol. 70, 245-255.

Altherr, R., Kreuzer, H., Lenz, H., Wendt, I., Harre, W., and Dürr, S., 1994. Further evidence for a Late Cretaceous low-pressure/high-temperature terrane in the Cyclades, Greece; petrology and geochronology of crystalline rocks from the islands of Donoussa and Ikaria: Chemie der Erde 54, 319–328.

Anderson, Don L. Theory of the Earth. Boston: Blackwell Scientific Publications, 1989.

Andriessen, P.A.M., Banga, G., Hebeda, E.H., 1987. Isotopic age study of pre-Alpine rocks in the basal units on Naxos, Sikinos and Ios, Greek Cyclades. Geologie en Mijnbouw 66, 3-14.

Audet, P., 2010. Temporal variations in crustal velocity structure near Parkfield, California, using receiver functions, Bull. Seism. Soc. Am., 100, 1356-1362.

Audet, P., 2015. Layered crustal anisotropy around the San Andreas Fault near Parkfield, California, J. Geophys. Res., doi:10.1002/2014JB011821, in press.

Avigad, D., 1993. Tectonic juxtaposition of blueschists and greenschists in Sifnos Island (Aegean Sea) – implications for the structure of the Cycladic blueschist belt, J. Struct. Geol. 15 (12), 1459–1469.

Babuska, V., 1972. Elasticity and anisotropy of dunite and bronzitite. J. Geophys. Res. 77, 6955– 6965.

Bachmann, F., Hielscher, R., Schaeben, H., 2010. Texture Analysis with MTEX – Free and Open Source Software Toolbox. Solid State Phenomena 160, 63-68.

Bascou, J., Barruol, G., Vauchez, A., Mainprice, D., and Egydio-Silva, M., 2000. EBSD-measured lattice-preferred orientations and seismic properties of eclogites. Tectonophysics 342, 61– 80.

Ben Ismail, W., and Mainprice, D., 1998. An olivine fabric database: an overview of upper mantle fabrics and seismic anisotropy, Tectonophysics 296, 145–157.

Berger, A., Schneider, D.A., Grasemann, B., Stockli, D.F., 2013. Miocene Pb-Zn-Ag mineralisation and magmatism in Lavrio, Greece. Terra Nova 25, 181-191.

Bezacier, L., Reyard, B., Bass, J.D., Wang, J., and Mainprice, D., 2010. Elasticity of glaucophane, seismic velocities and anisotropy of the subducted oceanic crust. Tectonophysics 494, 201–210.

Bianchi, I., Park, J., Agostinetti, N. P., and Levin, V., 2010. Mapping seismic anisotropy using harmonic decomposition of receiver functions: An application to Northern Apennines, Italy, J. Geophys. Res., 115, B12317, doi:10.1029/2009JB007,061.

Blake, M.C., Bonneau, M., Geyssant, J., Kienast, J.R., Lepvrier, C., Maluski, H., and Papanikolaou, D., 1981. A geological reconnaissance of the Cycladic blueschist belt, Greece: Geological Society of America Bulletin, 92, 247–254.

Bohnhoff, M., Makris, J., Papanikolaou, D., Stavrakakis, G., 2001. Crustal investigation of the Hellenic subduction zone using wide aperture seismic data. Tectonophysics 343, 239-262.

Bonneau, M., 1984. Correlation of the Hellenic nappes in the south-east Aegean and their tectonic reconstruction, in The Geological Evolution of the Eastern Mediterranean, edited by J. E. Dixon and A. H. F. Robertson, pp. 517 – 527, Blackwell Sci., Oxford, U. K.

Bostock, M. G., 1998. Mantle stratigraphy and evolution of the Slave province, J. Geophys. Res., 103, B9, 21183-21200.

Bröcker, M., Bieling, D., Hacker, B., Gans, P., 2004. High-Si phengite records the time of greenschist facies overprinting: implications for models suggesting mega-detachments in the

Aegean Sea. J. Metamorph. Geol. 22, 427-442.

Brown, J., Abramson, E., Angel, R., 2006. Triclinic elastic constant for low albite. Phys. Chem. Miner. 33(4), 256–265.

Brownlee, S., Hacker, B., Salisbury, M., Seward, G., Little, T., Baldwin, S., Abers, G., 2011. Predicted velocity and density structure of the exhuming Papua New Guinea ultrahigh-pressure terrane. J. Geophys. Res. 116, B08206.

Bruestle, A., 2012. Seismicity of the eastern Hellenic Subduction Zone, PhD thesis, Ruhr-Universität Bochum.

Cao, Y., Jung, H., Song, S., 2013. Petro-fabrics and seismic properties of blueschist and eclogite in the North Qilian suture zone, NW China: Implications for the low-velocity upper layer in subducting slab, trench-parallel seismic anisotropy, and eclogite detectability in the subduction zone. J. Geophys. Res. 118, 3037–3058.

Cassidy, J. F., 1992. Numerical experiments in broadband receiver function analyses, Bull. Seism. Soc. Am., 82, 1453–1474.

Chen, C.-C., Lin, C.-C., Liu, L.-G., Sinogeikin, S.V., Bass, J.D., 2001. Elasticity of single-crystal calcite and rhodochrosite by Brillouin spectroscopy. Am. Mineral., 86, 1525–1529.

Christensen, N., 2004, Serpentinites, Peridotites, and Seismology, International Geology Review 46(9), 795-816.

Cossette, É., Schneider, D., Audet, P., Grasemann, B., and Habler, G., 2015. Seismic properties and mineral crystallographic preferred orientations from EBSD data: Results from a crustal-scale detachment system, Aegean region, Tectonophysics, 651–652, 66–78.

Daeyeong, K., Katayama, I., Michibayashi, K., Tsujimori, T., 2013. Deformation fabrics of natural blueschists and implications for seismic anisotropy in subducting oceanic crust, Phys. Earth Planet. In. 222, 8–21.

Dempsey, E.D., Prior, D.J., Mariani, E., Toy, V.G., and Tatham, D.J., 2011. Mica-controlled anisotropy within mid-to-upper crustal mylonites: an EBSD study of mica fabrics in the Alpine Fault Zone, New Zealand. In: Prior, D.J., Rutter, E.H., Tatham, D.J. (eds) Deformation Mechanism, Rheology and Tectonics: Microstructures, Mechanics and Anisotropy. Geol. Soc, London, Special Publications 360, 33–47.

Dueker, K. G. and Sheehan, A. F., 1997. Mantle discontinuity structure from midpoint stacks

of converted P to S waves across the Yellowstone hotspot track, J. Geophys. Res., 102, 8313–8327.

Dürr, S., Altherr, R., Keller, J., Okrusch, M., and Seidel, E., 1978. Themedian Aegean crystalline belt: Stratigraphy, structure, metamorphism, magmatism, in Cloos, H., Roeder, D., and Schmidt, K., eds., Alps, Apennines, Hellenides: Stuttgart, Schweizerbart, p. 455–476.

Endrun, B., Meier, T., Lebedev, S., Bohnhoff, M., Stavrakakis, G., and Harjes, H.P., 2008. S-velocity structure and radial anisotropy in the Aegean region from surface wave dispersion. Geophys. J. Int. 174, 593–616.

Endrun, B., Lebedev, S., Meier, T., Tirel, C., and Friederich,W., 2011. Complex layered deformation within the Aegean crust and mantle revealed by seismic anisotropy. Nat. Geosci. 4, 203–207.

Erdman, M., Hacker, B., Zandt, G., and Seward, G., 2013. Seismic anisotropy of the crust: electron-backscatter diffraction measurements from the Basin and Range. Geophys. J. Int. 195, 1211–1229.

Evangelidis, C. P., Liang, W.-T., Melis, N. S., and Konstantinou, K. I., 2011. Shear wave anisotropy beneath the Aegean inferred from SKS splitting observations, J. Geophys. Res. 116, B04314, doi:10.1029/2010JB007884.

Fitz Gerald, J.D. and Stünitz, H., 1993. Deformation of granitoids at low metamorphic grade. I: Reactions and grain size reduction. Tectonophysics 221, 269–297.

Fouch, M. J., Fischer, K. M., Parmentier, E. M., Wysession, M. E., Clarke, T. J., 2000. Shear wave splitting, continental keels, and patterns of mantle flow, J. Geophys. Res., 105, B3, 6255-6275.

Frederiksen, A.W., and Bostock, M. G., 2000. Modelling teleseismic waves in dipping anisotropic structures, Geophys. J. Int., 141, 401–412.

Fujimoto, Y., Kono, Y., Hirajima, T., Kanagawa, K., Ishikawa, M., Arima, M., 2010. P-wave velocity and anisotropy of lawsonite and epidote blueschists: Constraints on water transportation along subducting oceanic crust, Physics of the Earth and Planetary Interiors 183, 219-228.

Grasemann B., Schneider D.A., Stöckli D.F., Iglseder C., 2012. Miocene bivergent crustal extension in the Aegean: Evidence from the western Cyclades (Greece). Lithosphere 4, 23–39.

Gautier, P. and Brun, J.P., 1994. Crustal-scale geometry and kinematics of late-orogenic extension in the central Aegean (Cylades and Evvia Island), Tectonophysics 238, 399-424.

Hatzfeld, D., Karagianni, E., Kassaras, I., Kiratzi, A., Louvari, E., Lyon-Caen, H., Makropoulos, K., Papadimitriou, P., Bock, G., and Priestley, K., 2001. Shear wave anisotropy in the upper mantle beneath the Aegean related to internal deformation, J. Geophys. Res. 106, 30737-30753.

Helbig, K., 1993. Simultaneous observation of seismic waves of different polarization indicates subsurface anisotropy and might help to unravel its cause, J. App. Geophys. 30, 1-24.

Hielscher, R., Schaeben, H., 2008. A novel pole figure inversion method: specification of the MTEX algorithm. Journal of Applied Crystallography 41, 1024-1037.

Hill, R., 1952. The elastic behaviour of a crystalline aggregate. Proceedings of the Physical Society of London 825, 349-354.

Huang, Z., Zhao, D., and Wang, L., 2011a, Frequency-dependent shear-wave splitting and multilayer anisotropy in northeast Japan: Geophys. Res. Lett. 38, 8. doi:10.1029/2011GL046804

Huang, Z., Zhao, D., and Wang, L., 2011b, Shear wave anisotropy in the crust, mantle wedge, and subducting Pacific slab under northeast Japan: Geochem. Geophys. Geosyst. 12, 1. doi:10.1029/2010GC003343

Hyndman, R.D. and Currie, C.A., 2011. Why is the North America Cordillera high? Hot backarcs, thermal isostasy, and mountain belts, Geology 39, 8, 783-786.

Iglseder, C., Grasemann, B., Rice, A.H.N., Petrakakis, K., Schneider, D.A., 2011. Miocene south-directed low-angle normal fault evolution on Kea (West Cycladic Detachment System, Greece). Tectonics 30, TC4013.

Ji, S., Shao, T., Michibayashi, K., Long, C., Wang, Q., Kondo, Y., Zhao, W., Wang, H., H. Salisbury, M., 2013. A new calibration of seismic velocities, anisotropy, fabrics, and elastic moduli of amphibole-rich rocks. J. Geophys. Res. 118, 4699–4728.

Jolivet, L. and Brun, J.-P., 2008. Cenozoic geodynamic evolution of the Aegean, Int. J. Earth Sci. 99, 109-138.

Jolivet, L., Faccenna, C., and Piromallo, C., 2009. From mantle to crust: Stretching the Mediterranean, Earth Planet. Sci. Lett. 285, 198–209.

Jolivet, L., Lecomte, E., Huet, B., Denèle, Y., Lacombe, O., Labrousse, L., Le Pourhiet, L., Mehl, C., 2010. The North Cycladic Detachment System. Earth Planet. Sci. Lett. 289, 87–104.

Jolivet, L., Faccenna, C., Huet, B., Labrousse, L., Le Pourhiet, L., Lacombe, O., Lecomte, E., Burov, E., Denèle, Y., Brun, J.-P., Philippon, M., Paul, A., Salaün, G., Karabulut, H., Piromallo, C., Monié, P., Gueydan, F., Okay, A.I., Oberhänsli, R., Pourteau, A., Augier, R., Gadenne, L., Driussi, O., 2013. Aegean tectonics: Strain localisation, slab tearing and trench retreat. Tectonophysics 597–598, 1-33.

Jung, H. and Karato, S., 2001.Water-induced fabric transitions in olivine, Science 293, 5534, 1460–1463.

Jung, S., Jung, H., Austrheim, H., 2014. Characterization of olivine fabrics and mylonite in the presence of fluid and implications for seismic anisotropy and shear localization. Earth, Planets Space 66, 46.

Katzir, Y., Matthews, A., Garfunkel, Z., Schnliestdt, M., and Avigad, D., 1996. The tectono-metamorphic evolution of a dismembered ophiolite (Tinos, Cyclades, Greece): Geol. Mag. 133, 237–25.

Kennett, B.L.N., 1983. Seismic wave propagation in stratified media, Cambridge University Press, UK, 285 pp.

Kennett, B.L.N., 1991. The removal of free surface interactions from three-component seismograms, Geophys. J. Int. 104, 153-163.

Kissel, C. and Laj, C., 1988. The tertiary geodynamical evolution of the Aegean arc: a paleomagnetic reconstruction, Tectonophysics 146, 183-201.

Kumazawa, M., Anderson, O.L., 1969. Elastic moduli, pressure derivatives, and temperature derivatives of single-crystal olivine and single-crystal forsterite. J. Geophys, Res. 74, 5961–5972.

Levin, V. and Park, J., 1997. P-SH conversions in a flat-layered medium with anisotropy of

arbitrary orientation, Geophys. J. Int. 131, 253-266.

Li, X., Bock, G., Vafidis, A., Kind, R., Harjes, H.-P., Hanka, W., Wylegalla, K., Meijde, M.v.d., and Yuan, X., 2003. Receiver function study of the Hellenic subduction zone: Imaging crustal thickness variations and the oceanic Moho of the descending African lithosphere, Geophys. J. Int., 155, 733– 748.

Lloyd, G., Butler, R., Casey, M., and Mainprice, D., 2009. Mica, deformation fabrics and the seismic properties of the continental crust. Earth Planet. Sci. Lett. 288, 320–328.

Lloyd, G., Butler, R., Casey, M., Tatham, D., Mainprice, D., 2011. Constraints on the seismic properties of the middle and lower continental crust. In: Prior, D., Rutter, E., Tatham, D. (eds) Deformation Mechanisms, Rheology and Tectonics: Microstructures, Mechanics and Anisotropy. Geol. Soc., London, Special Publications 360, 7–32.

Makris, J., Papoulia, J., and Yegorova, T., 2013. A 3-D density model of Greece constrained by gravity and seismic data, Geophys. J. Int., doi: 10.1093/gji/ggt059.

Mainprice, D., Bouchez, J.L., Blumenfeld, P., Tubia, J.M., 1986. Dominant C-slip in naturally deformed quartz: implications for dramatic plastic softening at high temperature, Geology 14, 812-822.

Mainprice, D., 1990. An efficient Fortran program to calculate seismic anisotropy from the lattice preferred orientation of minerals. Comput. Geosci. 16, 385–393.

Mainprice, D., Tommasi, A., Couvy, H., Cordier, P., Frost, D., 2005. Pressure sensitivity of olivine slip systems and seismic anisotropy of Earth's upper mantle. Nature 433, 731–733.

Mainprice, D., Ildefonse, B., 2009. Seismic anisotropy of subduction zone minerals - contribution of hydrous phases. Lallemand, S., Funiciello, F. Subduction zone geodynamics, Springer-Verlag, pp.63-84.

Mainprice, D., Hielscher, R., Schaeben, H., 2011. Calculating anisotropic physical properties from texture data using the MTEX open source package. In: Prior, D., Rutter, E., Tatham, D. (eds) Deformation Mechanism, Rheology and Tectonics: Microstructures, Mechanics and Anisotropy. Geol. Soc., London, Special Publication 360, 175–192.

McSkimin, H.J., Andreatche Jr., P., Thurston, R.N., 1965. Elastic moduli of quartz versus hydrostatic pressure at 25°and -195.8°C. J. Appl. Phys. 36, 1624–1632.

Meltzer, A., Christensen, N., 2001. Nanga Parbat crustal anisotropy: Implications for

interpretation of crustal velocity structure and shear-wave splitting, Geophys. Res. Lett. 28, 10, 2129-2132.

Morris, A. and Anderson, M., 1996. First palaeomagnetic results from the Cycladic Massif, Greece, and their implications for Miocene extension directions and tectonic models in the Aegean, Earth Planet. Sci. Lett. 142, 3, 397-408.

Moser, D.E., Cupelli, C.L., Barker, I.R., Flowers, R.M., Bowman, J.R., Wooden, J., Hart, J.R., 2011. New zircon shock phenomena and their use for dating and reconstruction of large impact structures revealed by electron nanobeam (EBSD, CL, EDS) and isotopic U–Pb and (U–Th)/He analysis of the Vredefort dome, Can. J. Earth Sci. 48, 117-139.

Nicolas, A. and Christensen, N., 1987. Formation of anisotropy in upper mantle peridotites: a review, Geodyn. Ser. 16, 111–123.

Porter, R., Zandt, G., and McQuarrie, N., 2011. Pervasive lower-crustal seismic anisotropy in Southern California: Evidence for underplated schists and active tectonics, Lithosphere 3, 3, 201–220.

Putlitz, B., Cosca, M.A., Schumacher, J.C., 2005. Prograde mica 40Ar/39Ar growth ages recorded in high-pressure rocks (Syros, Cyclades, Greece). Chem. Geol. 214, 79-98.

Reinecke, T., Altherr, R., Hartung, B., Hatzipanagiotou, K., Kreuzer, H., Harre, W., Klein, H., Keller, J., Geenen, E., Boger, H., 1982. Remnants of a Late Cretaceous high temperature belt on the island of Anafi (Cyclades, Greece). Neues Jahrbuch für Mineralogie Abhandlungen 145, 157-182.

Ring, U., Layer, P.W., and Reischmann, T., 2001. Miocene high-pressure metamorphism in the Cyclades and Crete, Aegean Sea, Greece: Evidence for large-magnitude displacement on the Cretan detachment, Geology 29, 5, 395-398.

Ring, U., Glodny, J., Will, T., and Thomson, S., 2011. Normal faulting on Sifnos and the South Cycladic detachment system, Aegean Sea, Greece. J. Geol. Soc. London 168, 751–768.

Savage, M. K., 1998. Lower crustal anisotropy or dipping boundaries? Effects on receiver functions and a case study in New Zealand, J. Geophys. Res., 103, 15069–15087.

Schliestedt, M., Matthews, A., 1987. Transformation of blueschist to greenschist facies rocks as a consequence of fluid infiltration, Sifnos (Cyclades), Greece, Contrib. Mineral. Petrol. 97, 237-250.

Schliestedt, M., Altherr, R., Matthews, A., 1987. Evolution of the Cycladic Crystalline Complex: Petrology, Isotope Geochemistry and Geochronology, Chemical Transport in Metasomatic Processes 218, 389-428.

Schneider, D.A., Senkowski, C., Vogel, H., Grasemann, B., Iglseder, C., 2011. Eocene tectonometamorphism on Serifos (western Cyclades) deduced from zircon depth-profiling geochronology and mica thermochronology. Lithos 125, 151–172.

Shearer, P.M., Introduction to seismology, Second Edition, Cambridge University press, 2009, 409 p.

Sherrington, H. F., Zandt, G., and Frederiksen, A., 2004. Crustal fabric in the Tibetan Plateau based on waveform inversions for seismic anisotropy parameters, J. Geophys. Res., 109, B02312, doi:10.1029/2002JB002345.

Shiomi, K., and J. Park, 2008. Structural features of the subducting slab beneath the Kii Peninsula, central Japan: Seismic evidence of slab segmentation, dehydration and anisotropy, J. Geophys. Res., 113, B10318, doi:10.1029/2007JB005,535.

Skarpelis, N., Tsikouras, B., and Pe-Piper, G., 2008. The Miocene igneous rocks in the basal unit of Lavrion (SE Attica, Greece): Petrology and geodynamic implications: Geol. Mag. 145, 1–15.

Smith, G.P., Wiens, D.A., Fischer, K.M., Dorman, L.M., Webb, S.C., and Hildebrand, J.A., 2001. A complex pattern of mantle flow in the Lau backarc, Science 292, 5517, 713–716. doi:10.1126/science.1058763

Sodoudi, F., Kind, R., Hatzfeld, D., Priestley, K., Hanka, W., Wylegalla, K., Stavrakakis, G., Vafidis, A., Harjes, H. P., and Bohnhoff, M., 2006. Lithospheric structure of the Aegean obtained from P and S receiver functions, J. Geophys. Res., 111, B12307, doi:10.1029/2005JB003932.

Sodoudi, F., Bruestle, A., Meier, T., Kind, R., Friederich, W. and EGELADOS working group, 2013. New constraints on the geometry of the subducting African plate and the overriding Aegean plate obtained from P receiver functions and seismicity, Solid Earth Discuss. 5, 427–461.

Tatham, D.J., Lloyd, G., Butler, R., Casey, M., 2008. Amphibole and lower crustal seismic properties. Earth Planet. Sci. Lett., 267, 118–128.

Thomson, C. J., 1996. Notes on waves in layered media to accompany program Rmatrix, In: Seismic waves in complex 3-D structures, Department of Geophysics, Charles University, Prague.

Tian, B.-F., Li, J. and Yao, Z.-X., 2008. Crustal anisotropy of Taihang Mountain Range using azimuthal variation of receiver functions, Acta Seismologica Sinica 21, 4, 358-369.

Tiberi, C., Diament, M., Lyon-Caen, H., and King, T., 2001. Moho topography beneath the Corinth Rift area (Greece) from inversion of gravity data, Geophys. J. Int., 145, 797– 808.

Tirel, C., Gueydan, F., Tiberi, C., and Brun, J.-P., 2004. Aegean crustal thickness inferred from gravity inversion. Geodynamical implications, Earth Planet. Sci. Lett. 228, 267–280.

Tomaschek, F., Kennedy, A., Villa, I.M., Lagos, M., Ballhaus, C., 2003. Zircons from Syros, Cyclades, Greece - recrystallisation and mobilisation of zircon during high-pressure metamorphism. J. Petrol. 44(11), 1977-2002.

Trotet, F., Jolivet, L., and Vidal, O., 2001. Tectono-metamorphic evolution of Syros and Sifnos Islands (Cyclades, Greece): Tectonophysics, 338, 179–206.

Vaughan, M., Guggenheim, S., 1986. Elasticity of muscovite and its relationship to crystal structure. J. Geophys. Res. 91, 4657–4664.

Walcott, C.R. and White, S.H., 1998. Constraints on the kinematics of post-orogenic extension imposed by stretching lineations in the Aegean region, Tectonophysics, 298, 155-175.

Ward, D., Mahan, K., Schulte-Pelkum, V., 2012. Roles of quartz and mica in seismic anisotropy of mylonites, Geophys. J. Int. 190, 1123–1134.

Wijbrans, J.R., Schliestedt, M., York, D., 1990. Single grain argon laser probe dating of phengites from the blueschist to greenschist transition on Sifnos (Cyclades, Greece). Contrib. Mineral. Petrol. 104, 582-593.

Wolfe, C. J., Solomon, S. C., 1998. Shear-Wave Splitting and Implications for Mantle Flow Beneath the MELT Region of the East Pacific Rise, Science, 280, 1230-1232.

Worthington, J.R., Hacker, B.R. and Zandt, G., 2013. Distinguishing eclogite from peridotite: EBSD-based calculations of seismic velocities, Geophys. J. Int. doi: 10.1093/gji/ggt004.

Zhong, X., Frehner, M., Kunze, K., and Zappone, A., 2014. A novel EBSD-based finite-element wave propagation model for investigating seismic anisotropy: Application to Finero Peridotite, Ivrea-Verbano Zone, Northern Italy, Geophys. Res. Lett., 41, 7105–7114, doi:10.1002/2014GL060490.

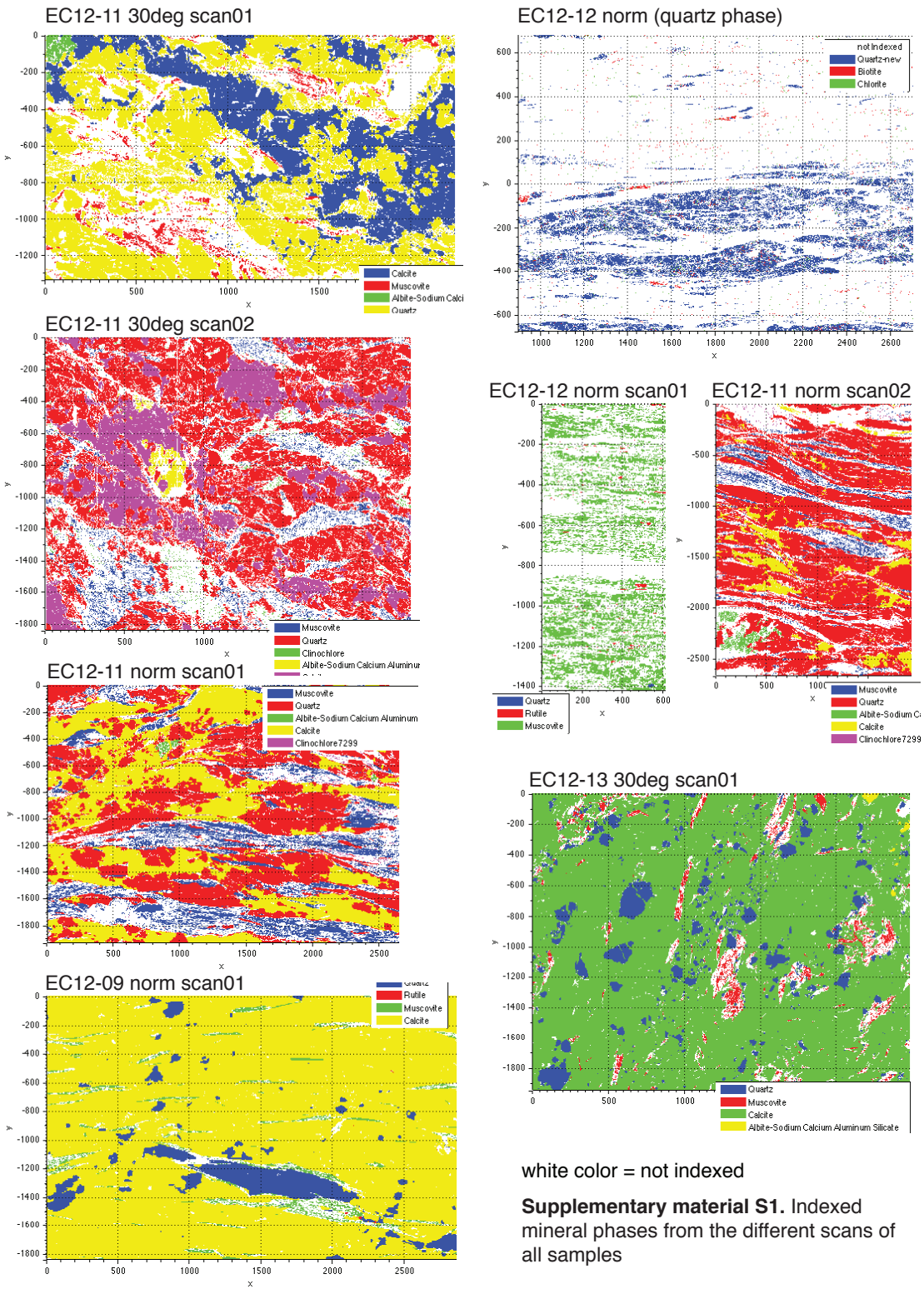

white color = not indexed

Supplementary material S1. Indexed mineral phases from the different scans of all samples

Supplementary material S1. Indexed mineral phases from the different scans of all samples

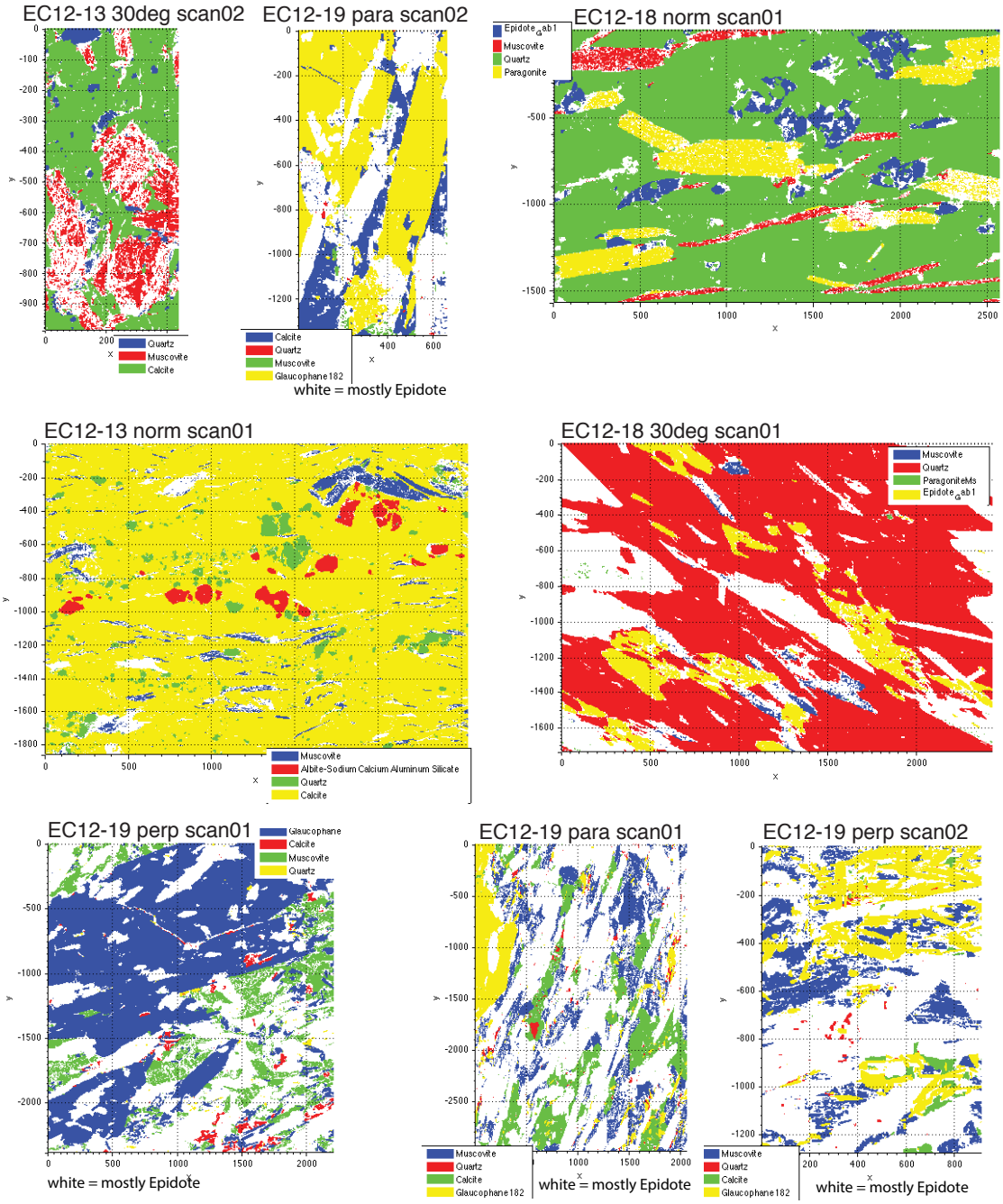

white color = not indexed

Supplementary material S2. Indexed mineral phases from the different scans of all samples

EC12-19 para

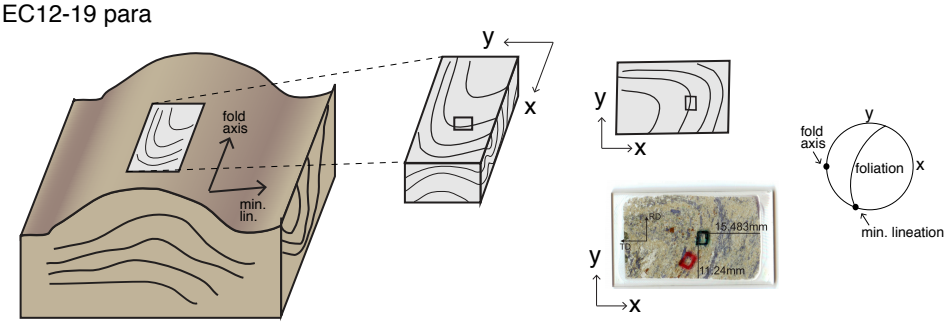

EC12-19 perp

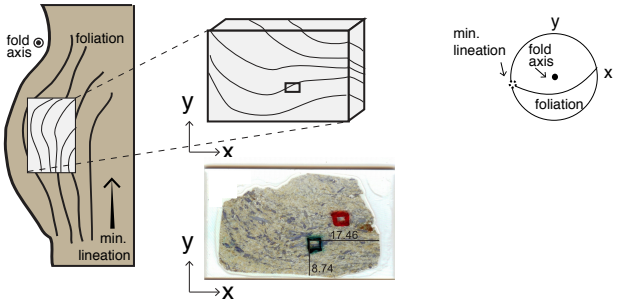

Supplementary material S3. Sketch of fold for sample EC12-19

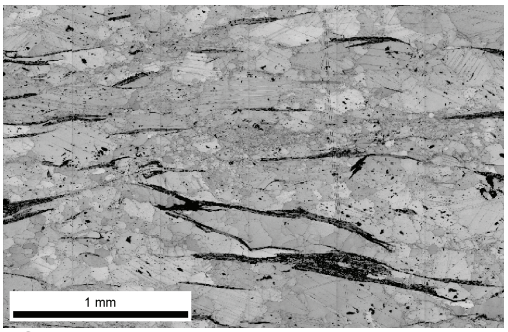

EC12-09 norm scan01

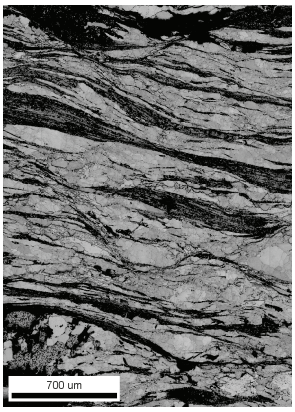

EC12-11 norm scan02

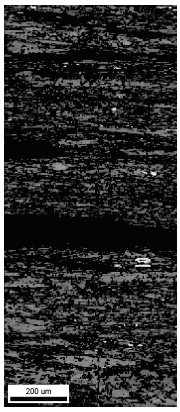

EC12-12 norm scan01

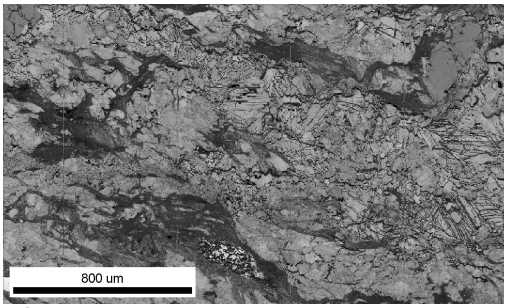

EC12-11 30deg scan01

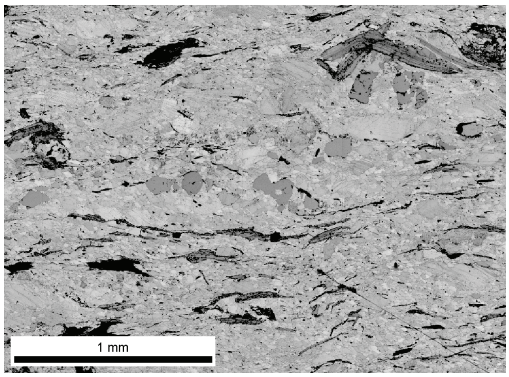

EC12-13 norm scan01

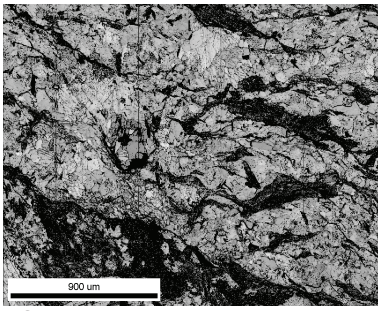

EC12-11 30deg scan02

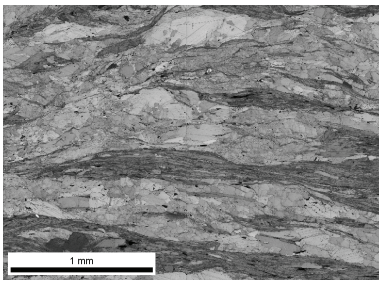

EC12-11 norm scan01

EC12-13 30deg scan02

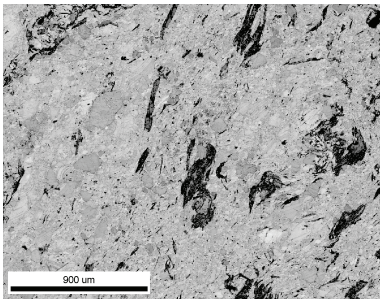

EC12-13 30deg scan01

Supplementary material S4. IQ maps of all scans describing the quality of an electron backscatter diffraction pattern. Darker gray shades in the image denote lower IQ values

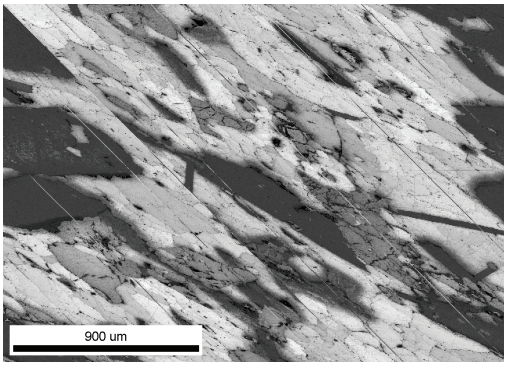

EC12-18 30deg scan01

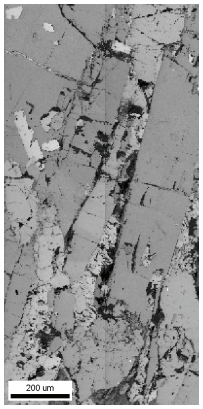

EC12-19 para scan02

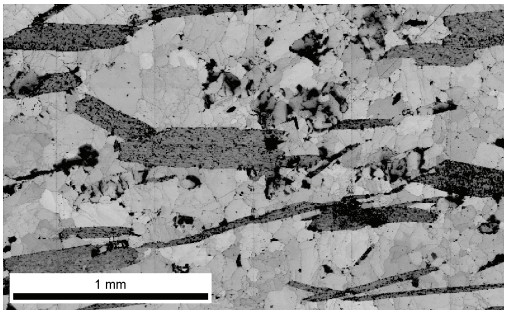

EC12-18 norm scan01

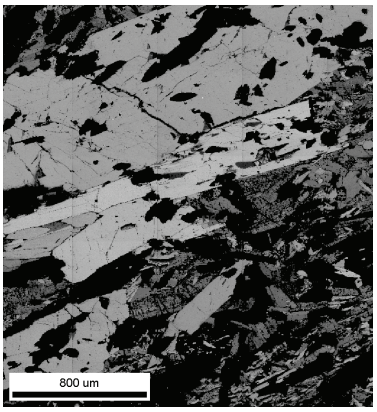

EC12-19 perp scan01

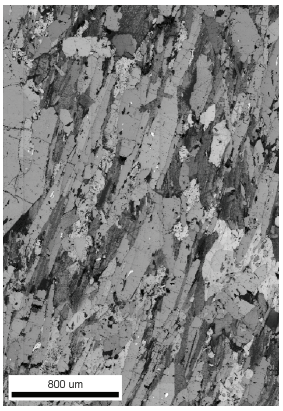

EC12-19 para scan01

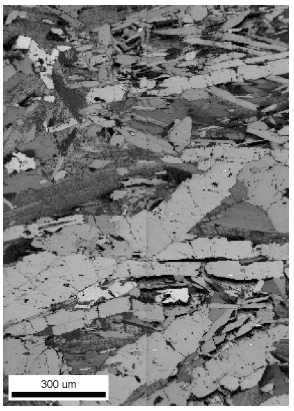

EC12-19 perp scan02

Supplementary material S5. IQ maps of all scans describing the quality of an electron backscatter diffraction pattern. Darker gray shades in the image denote lower IQ values

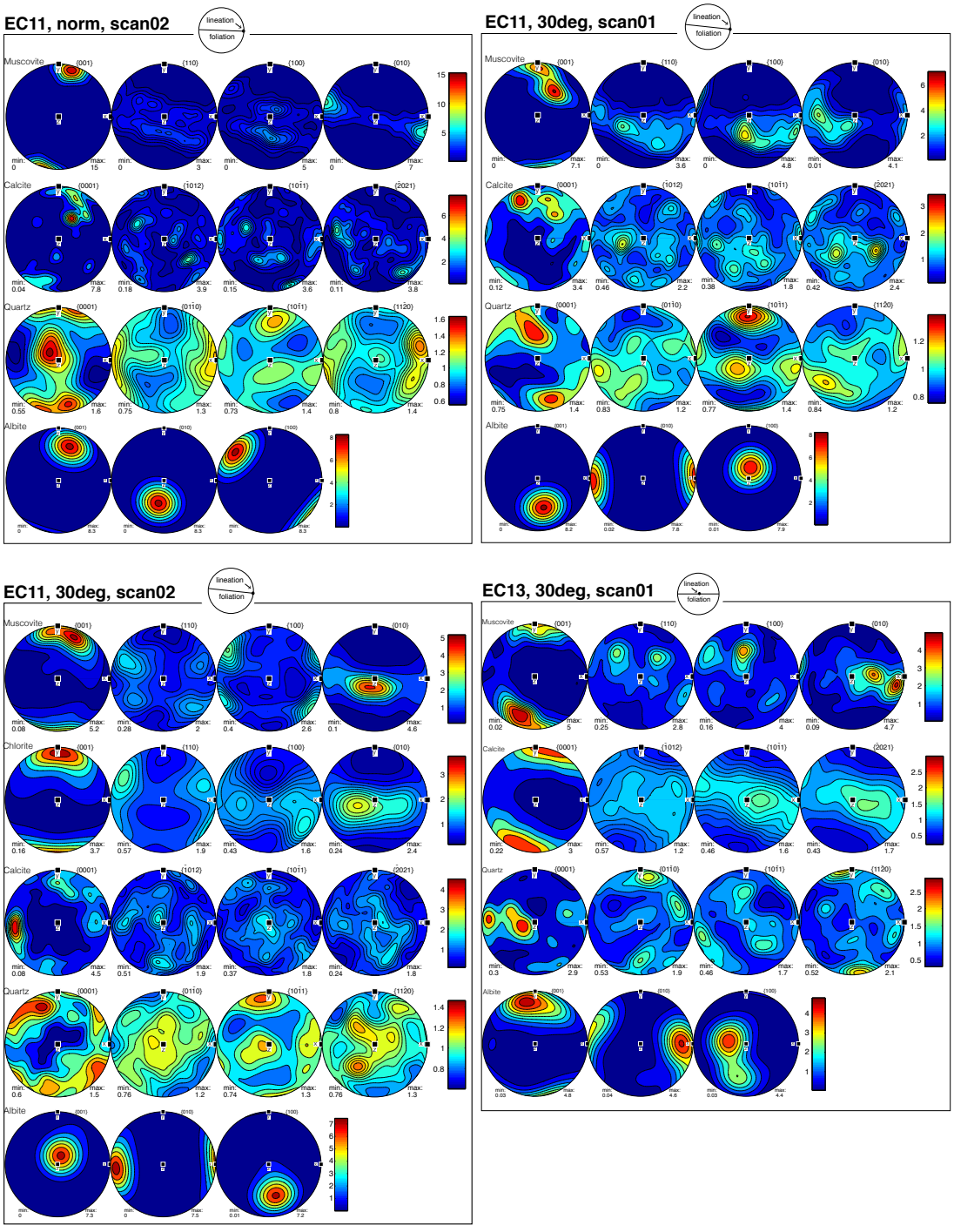

Supplementary material S6. Pole figures of minerals from other scans of this study's samples

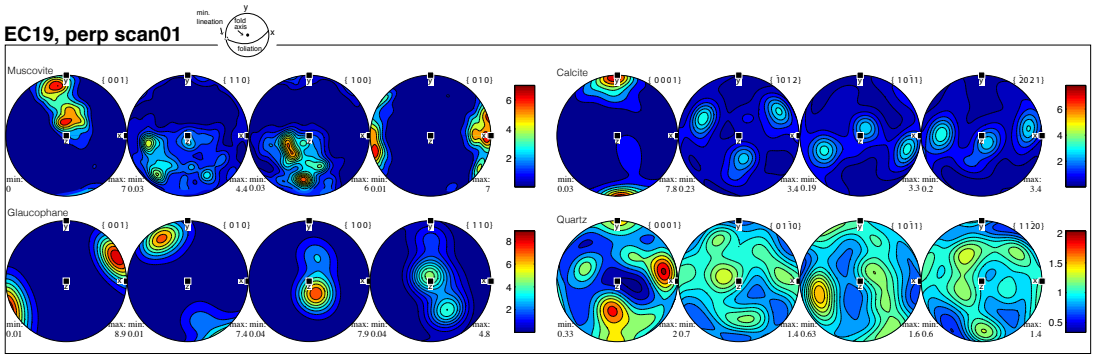

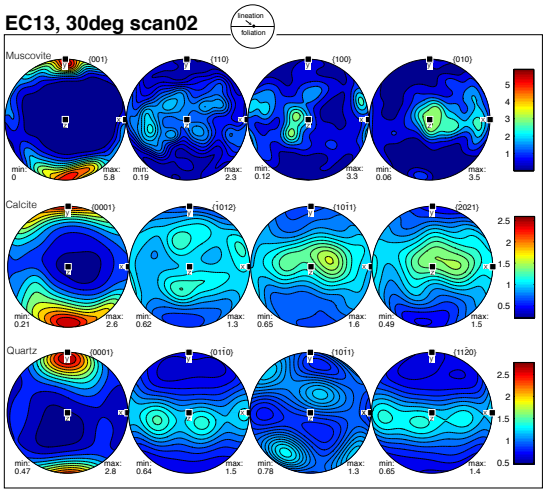

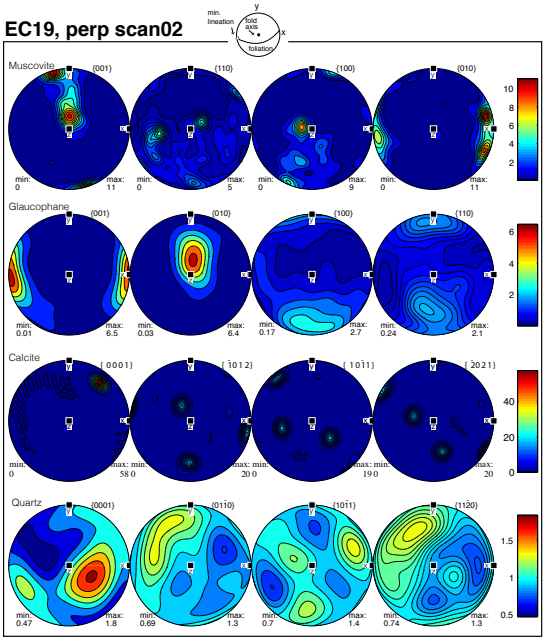

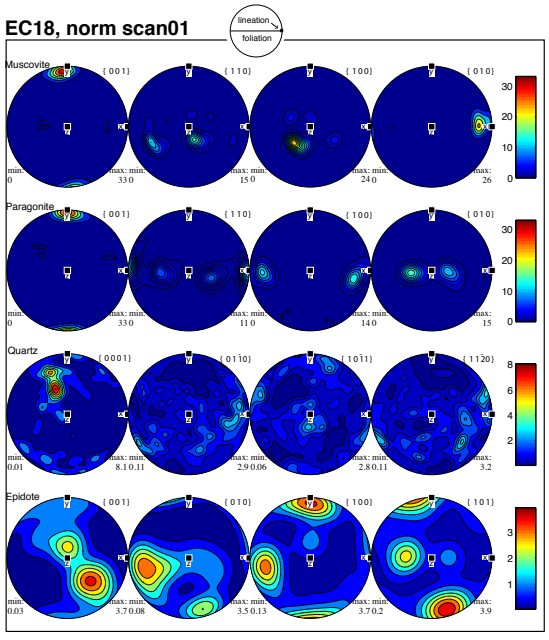

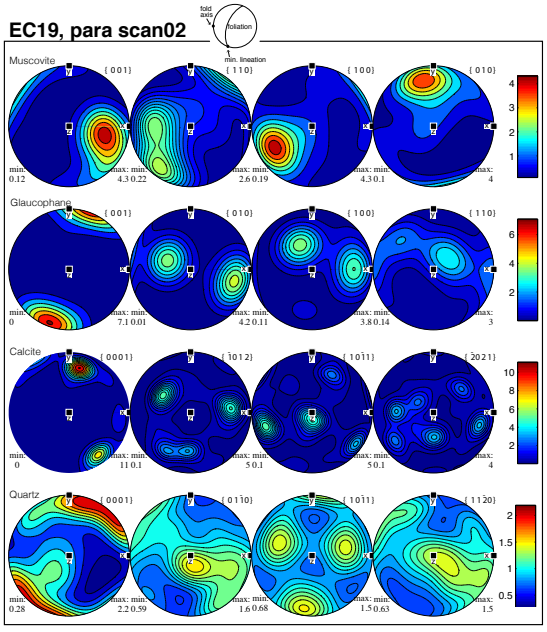

Supplementary material S7. Pole figures of minerals from other scans of this study's samples

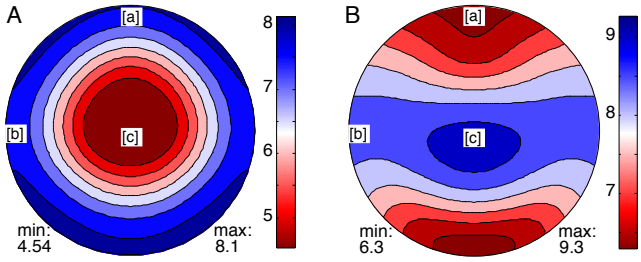

Supplementary material S8. P-wave velocity of single crystals for A: muscovite and B: glaucophane. Velocity in km/s.